Applied Energy 344 (2023) 121247

Contents lists available at ScienceDirect

Applied Energy

journal homepage: www.elsevier.com/locate/apenergy

Nonlinear operational optimization of an industrial power-to-heat system with a high temperature heat pump, a thermal energy storage and wind energy

Jasper V.M. Walden *, Martin Bähr, Anselm Glade, Jens Gollasch, A. Phong Tran, Tom Lorenz

German Aerospace Center, Institute of Low-Carbon Industrial Processes, Simulation and Virtual Design, Walther-Pauer-Straße 5, Cottbus, 03046, Brandenburg, Germany

GRAPHICAL ABSTRACT

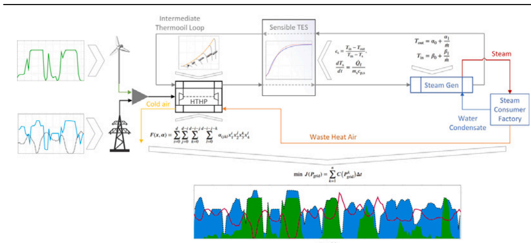

ARTICLE INFO

Keywords:
Operational optimization
Renewable steam generation
Electrification in industry
Offline optimization
Nonlinear programming

ABSTRACT

The heat demand for industrial processes is often provided in the form of steam generated by various fossil fueled equipment. In order to reduce CO_2 emissions, the heat demand has to be covered by renewable energy sources. Electrified steam generation relies on complex energy systems, that can be operated according to energy availability and cost developments. However, such a multi component industrial energy system poses a challenge in modeling and determining the cost- or emission-optimal operation of the system. This study develops a methodology to model a multi component industrial energy system on the basis of a case study. By optimal system operation, either costs or emissions are minimized in response to fluctuating renewable wind energy and electricity prices.

A high temperature heat pump (HTHP), a sensible thermal energy storage (TES) and a wind turbine are combined to create an electrified energy system to supply super-heated steam. During periods of low wind speed, additional grid electricity is purchased to ensure a steady heat supply. The HTHP offers a high operational flexibility and thus, enables the charging and discharging of the TES. A model of the closed reverse Brayton cycle HTHP, which is able to simulate part load behavior, is created in a process simulation software and consolidated in nonlinear surrogate models. The component behavior of a TES is represented by a combination of equations based on heat exchanger relations. Finally, the resulting algebraic nonconvex, nonlinear optimization problem based on the proposed system is solved using the local interior point optimizer (IPOPT) solver equipped with a multi-start approach to determine an optimal operation over a reference week with respect to the current wind power generation, grid emissions and electricity prices.

The results of the optimization show, that optimal operating strategies enable a high potential to decarbonize future industries at minimum operational costs or emissions.

* Corresponding author.
E-mail address: jasper.walden@dlr.de (J.V.M. Walden).

https://doi.org/10.1016/j.apenergy.2023.121247
Received 3 March 2022; Received in revised form 8 March 2023; Accepted 1 May 2023
Available online 19 May 2023

Nomenclature

Acronyms

ANOVA	Analysis of variance
C	Compressor
COP	Coefficient of performance
DLR	German Aerospace Center
DOE	Design of experiments
GWP	Greenhouse warming potential
HTF	Heat transfer fluid
HTHP	High temperature heat pump
HTHX	High temperature heat exchanger
HX	Heat exchanger
IEC	International Electrotechnical Commission
LTHX	Low temperature heat exchanger
NLP	Nonlinear programming
T	Turbine
TES	Thermal energy storage

Latin symbols

Δt	Discrete time step
$\dot{m}$	Mass flow
$\dot{m}_{III}$	LTHX inlet mass flow
$\dot{m}_{II}$	HTHX outlet mass flow
$\dot{m}_{IV}$	LTHX outlet mass flow
$\dot{m}_{I}$	HTHX inlet mass flow
$\dot{Q}$	Heat flow rate
$\dot{Q}_{s,ch}$	Storage heat flow rate during charge
$\dot{Q}_{s,dch}$	Storage heat flow rate during discharge
$c_{p,f}$	Heat capacity of thermo oil
$c_{p,s}$	Heat capacity of thermal storage
$g_{em,grid}$	Emission factor of elec. grid
$g_{pr,grid}$	Electricity price of elec. grid
m_s	Mass of thermal storage
N	Rotational speed compressor
P_{grid}	Electrical power of grid
P_{HTHP}	Electrical power of HTHP
P_{wt}	Electrical power of wind turbine
t	Time
T_1	Outlet temperature during charge
T_2	Inlet temperature steam generator
T_3	Outlet temperature steam generator
T_4	Storage outlet temperature during discharge
T_{III}	LTHX inlet temperature
T_{II}	HTHX outlet temperature
T_{IV}	LTHX outlet temperature
T_{I}	HTHX inlet temperature
T_s	Storage temperature

Greek symbols

α, β	Function coefficients
ϵ	Effectiveness
γ	Relaxation parameter
μ	Average value

1. Introduction

The majority of the energy required within industrial processes is heat [1], which is often provided as steam at elevated temperature and pressure [2]. Steam is the dominant heat transfer medium and therefore represents an essential part in almost all industrial branches. It can be found in e.g. the chemical industry, paper production or the food industry. Temperatures, at which steam is utilized vary largely between 100 °C and 500 °C [3]. A similar variation applies for the amount of heat transported by steam. Industrial steam generators can deliver heat flow rates from a few kilowatt to more than 100 megawatt. In conventional plants, steam is generated by burning fossil fuels, which represents the main source of CO_2 emissions within the process. Thus, electrifying process heat is a first step towards reducing the industrial CO_2 emissions [4,5].

The growing interest in replacing industrial fossil fuel plants with renewable energy sources poses an economic and environmental challenge. One of the key challenges is cost. The natural gas prices for an industry consumer in Germany were approximately 2.6 €-cent/kWh in 2018 [6], while the price of electricity was at an average of 15 €-cent/kWh [7]. This means, that an electrified system would have to be more than 5 times as efficient to equalize costs. However, due to the fluctuating energy generation by renewable energy sources, an electrified system with a storage could take advantage of lower electricity prices and thus improve the economic feasibility. In combination with a heat pump with a high part load capability [8], a great improvement in energy efficiency can be achieved. A similar problem, when competing with a conventional industrial energy system, arises for the CO_2 emissions. The German electricity grid has a high CO_2 footprint, in comparison with the combustion of natural gas, thus an electrified system has to be very efficient to generate less emissions.

Currently, the German Aerospace Center (DLR) Institute of Low Carbon Industrial Processes develops a HTHP prototype based on the reverse Brayton cycle allowing for high temperature heat supply at temperatures up to 350 °C [8,9]. The heat pump technology is of particular interest to the industry because of its ability to up-cycle waste heat, which would otherwise remain unused.

Previous work on the electrification of industry has been carried out by Bühler et al. [10], who investigated several strategies for electrifying industrial processes with either a heat pump or an electrical boiler integration. In most studies a vapor compression heat pump is integrated. However, this study utilizes a Brayton cycle heat pump due to its flexibility at part loads and its ability to acquire sensible heat from the heat source. The relevance of both these factors is significant to the evaluated application. Further research, on the direct and indirect electrification strategies in chemical industry, was carried out by Chen [11]. Zhang [12] modeled a grid-connected factory with onsite PV and battery systems. The electricity cost of the factory were optimized as a mixed integer program, improving the scheduling strategy. However, the optimal operation is not examined.

Optimal operation problems of energy systems have been formulated for a variety of problems, e.g. smart micro grids & community energy networks [13–15] and district heating [16,17]. Studies are often based on the Energy Hub concept [18–21] or similar methods, such as the standardized matrix modeling method, which Li et al. [14] applied for a community energy network. Most of the studies mentioned use linear models to circumvent the nonlinearities in the component modeling. However, the specific, nonlinear characteristics of each component can have a significant impact on the behavior and operating scheme. Tian [22] demonstrated the influence on the operational cost by an improved simulation model. Nowadays, nonlinear properties of components are typically considered in energy system modeling such as [23–27].

The respective continuous optimization problem is usually converted into a nonlinear programming (NLP) problem by time discretization, which present a challenge for the computation of the numerical solution. Due to the complexity of such models, deterministic global methods for obtaining optimal solutions are generally not suitable in practice, so that local methods are often applied [28–30]. However, since suboptimal local solutions can distort the evaluation of the underlying operating strategy, local methods can be coupled with a multi-start procedure to determine a more optimal control strategy, as exemplary used in [31–33]. An alternative approach to obtain a global solution of NLP formulations is often based on linearization methods, see e.g. [15,34,35].

The present research explores the optimal operation of an innovative electrified industrial energy system by utilizing comprehensive and nonlinear models of its components in the optimization process. Moreover, the investigation incorporates historical records of wind velocity, electricity pricing, and electricity grid emissions. Consequently, the aim of this study is to formulate an optimization problem with nonlinear component models and detailed system constraints in the algebraic modeling language GAMS [36]. The focus is to calculate an optimized operating scheme for a reference week including the datasets for the alternating cost of electricity and the wind power generation based on present wind speeds.

The optimization problem is formulated using a case study with a conceptual electrified energy system. The HTHP is simulated with respect to its part load behavior. In particular, the compressor is modeled with a scaled performance map and the turbine is operated with a constant corrected mass flow. The entire operating range of the HTHP is mapped into an algebraic form using polynomial surrogate models. Furthermore, a novel lumped capacitance model of the TES is developed.

Combining the created models, an algebraic nonlinear optimization problem of the case study is formulated. The resulting model is optimized in GAMS using the interior point optimizer [37] with numerous initial values to minimize the operational cost or CO_2 emissions of a reference week.

2. Industrial energy system and modeling

Electrified industrial energy systems, which are driven by renewable energies, come along with the challenge of determining an optimal operation scheme due to the fluctuating electricity generation by renewable energies and a constant heat requirement of the industrial process. A storage and additional grid power is required to cover short and long phases of low feed in energy by the renewable source. We present an industrial energy system shown in Fig. 1, which is supplied with electrical energy by an on-site wind turbine and a connection the electrical grid. A closed Brayton cycle high temperature heat pump generates heat from electricity. Furthermore, a thermal energy storage is integrated between the HTHP and the industrial consumer.

In the considered case study, the constant heat demand of an industrial consumer has to be satisfied. The heat is supplied as superheated steam at 13 bar and 215 °C. The temperature, pressure and mass flow rate of the heat demand is chosen to be comparable to the data of a conventional industrial gas boiler [38].

The HTHP supplies high temperature process heat to an intermediate loop that can be routed through a sensible TES. The heat transfer fluid (HTF) in the intermediate loop is chosen to be a thermal oil, due to its compactness and fluid phase within the temperature range. The routing of the HTF determines the operation of the TES. During discharging operation, the HTF is heated in the TES before entering the steam generator. Charging operation is vice versa. In idle operation, the HTF bypasses the TES entirely.

Marina et al. [39] states that the majority of the waste heat of industrial processes is within the interval of 40–100 °C. The present study assumes waste heat temperature levels between 60–100 °C as heat source temperature for the HTHP. The waste heat is considered to be dry air.

The following sections describe the modeling of the system components. The proposed system (cf. Fig. 1) is based on the following technical assumptions and simplifications:

- Pressure, friction and heat losses are neglected. Similarly, the power consumption of auxiliary systems, such as pumps for secondary cycles, is disregarded.
- The positive impact of selling excess wind power is not taken into account.
- Operation and maintenance cost of the wind turbine are assumed as 1.2 ct per kWh according to an estimation of the European Wind Energy Association [40].
- The system is considered to be in quasi-steady states at all times. We neglect the dynamic behavior of the components during a change of operating conditions. Sass et al. [25] states that quasi-steady state assumptions can be adequate, if ramp constraints are added. However, for our scenario ramp constraints are not considered.
- In addition to providing heat, the closed Brayton cycle HTHP generates cold air. However, in the current scenario no constraints are imposed on the cold outlet stream, thus disregarding potential cooling applications.

It should be emphasized that the design optimization is not considered in this study. The optimal size of each component and the process structure is a different optimization problem, which needs to be addressed in a separate study.

2.1. High temperature heat pump model

The incorporated high temperature heat pump operates on the basis of the recuperated, closed reverse Brayton cycle. This design is in line with the development work of the DLR Institute of Low-Carbon Industrial Processes, which is currently building a pilot plant of the mentioned high temperature heat pump.

Compared to the pilot plant, the capacity of the HTHP is vastly increased. However, in order to keep the component dimensions within a moderate scale, it is assumed that three high capacity HTHPs will run in parallel. Furthermore, the HTHP and its turbo machinery offer a high operational flexibility to adapt its heat rejection and heat addition to the present demand. Detailed investigations on the operational flexibility of the Brayton cycle HTHP have been carried out by Oehler et al. [8].

Fig. 2 presents the schematic flow sheet of the reverse Brayton cycle heat pump. The associated T-s diagram is shown in Appendix A. The cycle consists of five key components. Air is used as the working medium due to its availability, low cost and low greenhouse warming potential.

At state (a), air is drawn into the compressor. The gas is compressed and thus the temperature increases. The working fluid proceeds to the high temperature heat exchanger (HTHX), where heat is transferred from the working fluid to the HTF (I–II).

The remaining heat of the working fluid is then used for internal heat recovery in the recuperator. Downstream of the recuperator (c), a turbine expands the pressurized fluid, while recovering power and cooling the fluid down. The resulting stream (d) is then heated in the low temperature heat exchanger (LTHX) by residual process heat (III). After passing through the recuperator, the working medium enters the compressor again at state (a).

The outlined cycle is simulated within the process simulation software Ebsilon [41]. The design parameters, as shown in Table 1, are selected to allow a realistic representation of an industrial-scale heat pump.

Compressor. The compressor is modeled using a scaled compressor map of an axial aero-engine booster provided by Converse [42]. The employed compressor map consists of tables stating values for corrected mass flow rate, total pressure ratio, isentropic efficiency and corrected relative speed. Scaling factors are applied to the original compressor map data, so that the scaled map represents a compressor satisfying the design point defined in Table 1. The HTHP's operating points in the compressor map are presented in Fig. 3.

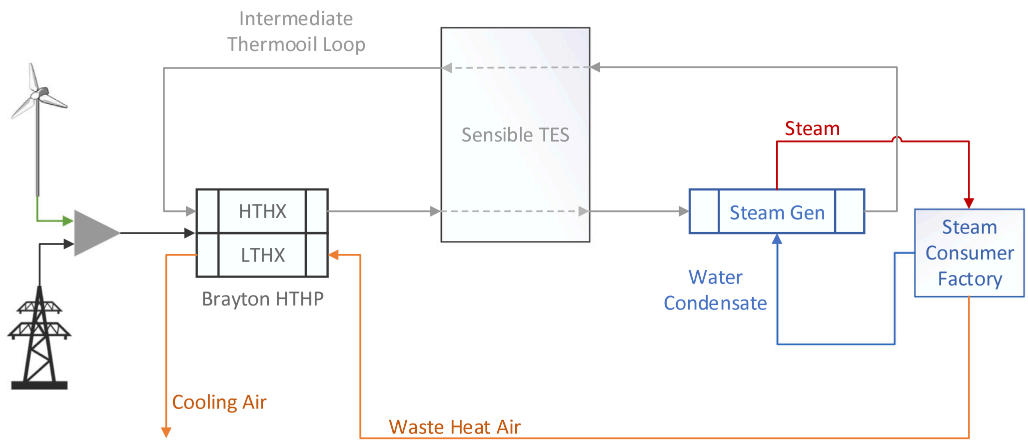

Fig. 1. Schematic diagram of the investigated industrial energy system for steam generation. The system incorporates a HTHP, a TES and a steam generator powered by electricity from a wind turbine or if necessary, the power grid. The HTHP can charge the TES with an intermediate thermo oil stream and uses a waste heat air stream at 75 °C as heat source. If the TES discharges, the HTHP's power consumption is reduced significantly, because less heat has to be supplied to the intermediate loop in order to ensure constant steam generation.

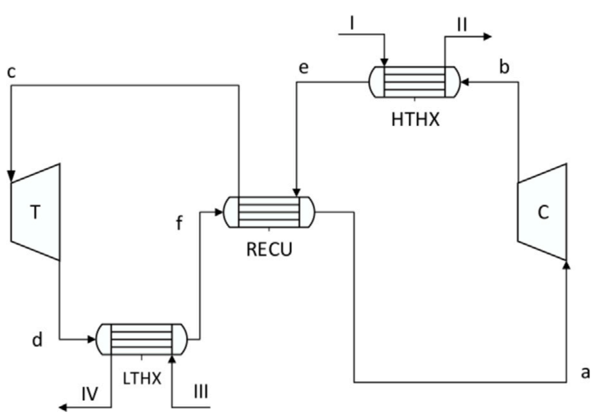

Fig. 2. Flow sheet diagram of the recuperated reverse Brayton cycle including secondary streams. The letters relate to the T,s-diagram shown in Appendix A.

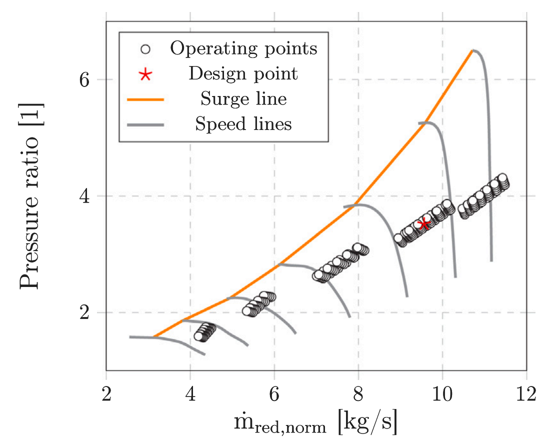

Fig. 3. The applied compressor map including the surge line, speed lines and the operating points of the HTHP.

Table 1
Design point parameters of the HTHP.

Component	Value
Rated power [MW]	1.06
Compressor isentropic efficiency [%]	85
Turbine isentropic efficiency [%]	90
Motor & Generator efficiency [%]	100
Heat exchanger effectiveness [%]	90
Recuperator effectiveness [%]	85
Temperature of heat source [°C]	75
Mass flow rate of heat source [kg/s]	5
Temperature of heat sink [°C]	300
Mass flow rate of heat sink [kg/s]	6.256
Pressure ratio [–]	3.5
Primary mass flow [kg/s]	7.315
COP_{real} [–]	1.45
COP_{ideal} [–]	2.55
$\zeta = \frac{COP_{real}}{COP_{ideal}}$ [%]	57

Turbine. The entire operating range examined in this study is assumed to be within the choke regime, where sonic flow speed is reached in the narrowest turbine cross section. The corrected mass flow rate at the turbine inlet can be assumed to be constant. According to Walsh [43], the choke regime includes most of the turbine's operating range, especially the high-power range. The turbine is sized by applying a corrected mass flow rate that invokes sufficient compressor surge margins for all operating points. In addition, it is assumed for simplicity purposes that the isentropic efficiency is constant for all turbine operating points.

Heat exchangers. The heat exchangers are designed by an effectiveness approach [44]. By defining the effectiveness, the nominal values for heat transfer coefficient U and HX area A are calculated in Ebsilon. These values are used to calculate the exchanged heat duty during part-load operation.

2.2. Steam generator

The mass flow rate and temperature of the heat transfer fluid is depending on the operating condition of the system. For a variety of mass flow rates and temperatures a data set for the outlet conditions of the HTF is calculated in Ebsilon. The resulting dataset is used to derive a surrogate model of the steam generator, see Section 3.1.2. Within the steam generator, a constant minimum value for the pinch point of 5 K is set.

2.3. Thermal energy storage model

In the present temperature range of 100–400 °C many different TES solutions can be considered [45–48]. Due to their high heat capacity, market availability as well as low investment and maintenance cost,

Table 2
Mean values for thermal properties of Heatcrete [53] and Therminol VP-1 [54] at 300 °C.

	Heatcrete	Therminol VP-1
Thermal conductivity [W/mK]	1.92	0.096
Specific heat capacity [kJ/kgK]	1.025	2.314
Density [kg/m^3]	2260	817

concrete-based TES modules are selected [49–51]. The following Sections describe the details of the thermal energy storage modeling and the verification of the model.

2.3.1. Modeling

Most sensible TES can be modeled with a discretized finite element approach using Newton's law of cooling to calculate the transferred heat and different formulations of energy conservation to account for the resulting temperature change on both sides. However, in this work, a reduced model of the TES, which is not reliant on solving the spatial discretization, is developed to reduce calculation time during the optimization for optimal operation. Nonetheless, the behavior of the reduced model is still similar to that of a spatially discretized model.

The model is developed using a lumped capacitance approach [46, 52], in which a uniform TES temperature is assumed. This approach takes advantage of the storage's heat exchanger functionality and reduces the TES model to a two-equation-system.

The maximum transferred heat flow rate $\dot{Q}_{\mathrm{max}}$ is determined by the lower heat capacity of both fluids, so that the effectiveness results in

$$\epsilon = \frac{\dot{Q}_{\mathrm{real}}}{\dot{Q}_{\mathrm{max}}} = \frac{c_{\mathrm{p,i}}\dot{m}_i(T_{\mathrm{i,in}} - T_{\mathrm{i,out}})}{[c_{\mathrm{p}}\dot{m}]_{\mathrm{min}}(T_{1,\mathrm{in}} - T_{2,\mathrm{in}})} \tag{1}$$

Indices 1 and 2 indicate the fluid on each side of the heat exchanger. The index *min* indicates the smaller product of $c_{\mathrm{p}}\dot{m}$.

However, for industrial size heat storage's the storage mass is usually big enough to set the fluid's heat capacity as limiting factor in the denominator. Thus, Eq. (1) can therefore be reduced to

$$\epsilon_{\mathrm{s}} = \frac{T_{\mathrm{in}} - T_{\mathrm{out}}}{T_{\mathrm{in}} - T_{\mathrm{s}}}. \tag{2}$$

Simulating the TES behavior with a given input temperature of the HTF T_{in} and a given mean storage temperature $T_{\mathrm{s},t}$ at time step t, Eq. (2) yields the outlet temperature T_{out}.

Under ideal conditions, the heat rejection of the fluid $\dot{Q}_{\mathrm{f}}$ equals the heat addition to the storage $\dot{Q}_{\mathrm{s}}$, which allows the calculation of the resulting storage temperature change by the following equation:

$$\frac{\mathrm{d}T_{\mathrm{s}}}{\mathrm{d}t} = \frac{\dot{Q}_{\mathrm{f}}}{m_{\mathrm{s}}c_{\mathrm{p,s}}} \tag{3}$$

2.3.2. Model verification

The geometry of the TES module used for the model's verification is a long cylinder, centrally penetrated by a single tube carrying the HTF. Hoivik et al. [51] also used this geometry to validate their numerical simulation for cylindrical TES with multiple HTF passages. It is presumed that the storage considered in the presented energy system is comprised of multiple such modules connected in parallel. Thus, modeling one module represents the behavior of the entire storage system. To assure scalability, the ratio between the storage mass and mass flow rate through the storage must be equal for the verification model and the full size model.

Table 2 shows mean thermal properties of the material and HTF chosen for the verification simulation.

The model has been verified with a temporally and spatially discretized model [41] based on 2D heat transfer equations in Ebsilon. The used heat transfer coefficient is calculated with the Dittus–Boelter-approximation [55]. Parameters used for the verification simulation are shown in Table 3. Simplifications have been made in neglecting all heat losses occurring between the concrete elements and to the environment.

Table 3
Simulation parameters of the verification case.

Parameter	Verification value
Storage length [m]	77
Storage diameter [m]	0.25
Fluid passage diameter [m]	0.021
Storage mass [kg]	1960
HTF mass flow [kg/s]	0.065
Effectiveness [–]	0.9
Heat transfer coefficient [W/(m^{2}K)]	520.96
Cells in axial direction (Ebsilon)	30
Cells in radial direction (Ebsilon)	5
Simulation time step [h]	1

Table 4
Error metrics for the verification case.

	Mean relative error [%]	Mean absolute error [K]
Discharge		
T_{s}	2.2	4.75
$T_{\mathrm{out,HTF}}$	1.58	3.75
Charge		
T_{s}	1.82	6.03
$T_{\mathrm{out,HTF}}$	1.44	4.57

Furthermore, a time step of 1 h proved to be sufficiently small to render the discretization error insignificant.

Fig. 4 shows the HTF outlet temperature and the storage temperature when charging from 200 °C to 350 °C. Similar studies were conducted for charging and discharging processes. The discharging process can be found in Appendix B. While errors are inevitable due to the neglection of temperature gradients inside the storage and coarse temporal discretization, the new effectiveness model is able to predict the thermal behavior of the storage with sufficient accuracy. Table 4 shows the error metrics of the verification case, which are below 2.2%. A parity plot of the verification can be found in Appendix B. The TES can be reasonably well modeled with the proposed approach, replacing the need for a more complex model.

2.3.3. Fluid flow regulation

To ensure a constant heat supply for the steam generator a controllable HTF fluid bypass for the storage module is included, in which part of the fluid flow is split off before entering the TES and rejoins the main stream after circumventing the storage. The heat transferred to the TES is controlled by the flow split. This additional degree of freedom allows for a flexible operation of the TES. A bypass is implemented for charging and discharging cycles (cf. Fig. 6).

2.4. Wind turbine model

The wind speeds at hub height are of crucial importance as an input for a precise wind power prediction. The extrapolation of the wind speed is based on the vertical wind profile, which is related to two mathematical models, the logarithm and the power laws, cf. [56].

After extrapolating the wind speed to the corresponding hub height, the power curve, a wind turbine specific function, determines the generated wind power as a function of the wind speed. By using power curves, the electrical power output can easily be predicted without detailed knowledge of the operation and control of the turbine.

2.5. Data

For the present case study, we assume that the industrial process is located in Hoyerswerda, Germany. For this scenario, measured wind speeds can be taken from the German Weather Service [57], which has a weather station at this location. Hoyerswerda is characterized by low

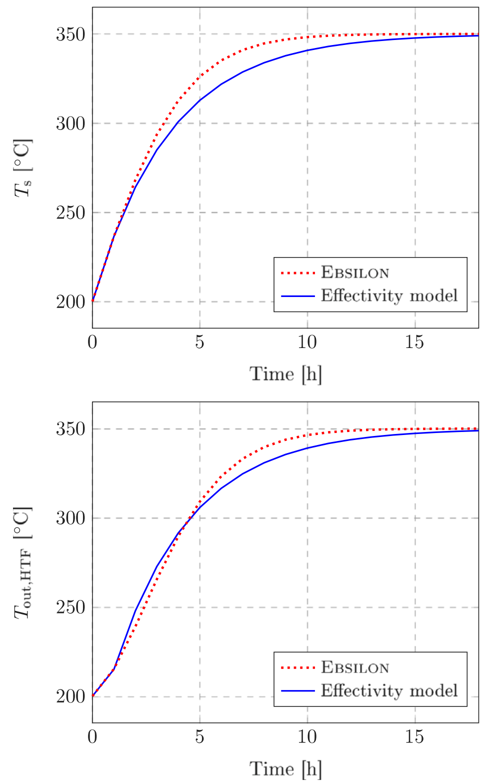

Fig. 4. Storage temperature and HTF outlet temperature during the charging process. The parameters involved in the verification simulation are shown in Table 3. The discharge process also shows (see Appendix B) that the effectiveness model is well suited.

average wind speed conditions, consequently a wind turbine designed for low wind speeds (IEC IIIB) is chosen. More precisely, a model of a Vestas V150 [58] wind turbine is used, which has a maximum capacity of 4.2 MW and a hub height of 166 m.

To determine the generated wind power, the hourly wind speed data is extrapolated using the power law [56]. According to the IEC standards, all power curves are normalized to a reference density. Therefore, the power output must be adapted to the corresponding hub height using the barometric height formula [59]. However, we neglect this here, as it has only a very small influence in this context.

For cost- or emission-optimized system operation, the electricity price and the emission factor of electricity generation mix are required. The electricity price and the individual electricity generation sources are available in the public domain and are provided by the ENTSO-E TP [7,60]. The CO_2 grid emissions of the power generation mix are derived from all individual emission factors and their share in power production within the associated hour. Afterwards, their sum is divided by the total electricity production. The respective emission factors are taken from [61].

The conducted case study in Section 4 is based on the reference week 27.07.2020–02.08.2020. This week was chosen due to its changing wind conditions, positive electricity prices and, at the same time, realistic grid emissions of the power mix in the context of 2020. Fig. 5 shows the average grid emissions and electricity price of the selected week $\mu_{ref,week}$ in the context of the hourly price and emission data of 2020 and the mean values μ_{year} for 2020.

3. Surrogate models and mathematical formulation

In this section, we explain how the proposed multi-component system is transferred into an algebraic optimization problem in order

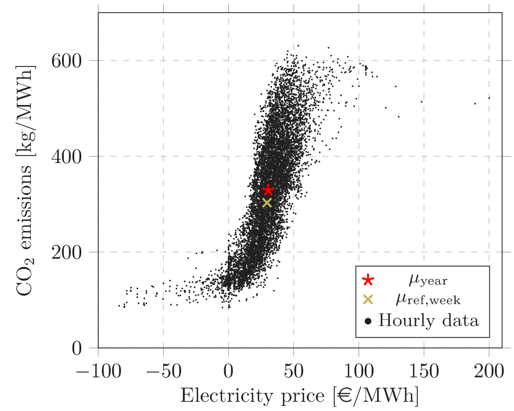

Fig. 5. The selected reference week 27.07.2020–02.08.2020 in the context of the 2020 grid data. The averaged hourly data of the electricity grid is indicated by the black dots and the red star indicates the yearly average values within 2020. The yellow cross represents the average value during the reference week.

to study its cost- and emission-optimal operation. To integrate the EBSILON simulation of the HTHP and the steam generator into the overall optimization problem, in an algebraic form, analytical surrogate models are created. Surrogate models mimic the input–output-behavior of the system components. The created equations are then coupled with the TES model, so that the mathematical optimization problem can finally be formulated.

3.1. Surrogate models

Surrogate-based modeling approaches [62–64] are a popular technique to approximate the predictions of an underlying complex simulation-based model as accurately as possible. In the present work, these models consist of algebraic functions, which offer two main advantages: First, such models help to avoid complicated software couplings by replacing the EBSILON simulation with a set of functions, that can easily be implemented into the overall model in GAMS. Additionally, they prevent the use of challenging simulation-based optimization techniques [65].

In the technical implementation for creating the surrogate models mentioned, we follow a classic and systematic procedure called design of experiment (DOE) [66]. In general, the DOE process consists of three main steps: determining the objectives and the independent variables (input sample), planning the experimental design over the design space and conducting the real-world experiment or simulations (output sample) at design points. Finally, we construct the surrogate models from the created sample data and evaluate their coefficient of determination.

3.1.1. High temperature heat pump surrogate model

In general, a surrogate model describes how a chosen value depends on a set of independent variables, refered to as factors. As for the HTHP simulation, three objective values were chosen, namely: (i) the consumed electrical power P_{HTHP}, (ii) the outlet oil temperature T_{II} of the HTHX and (iii) the outlet air temperature T_{IV} of LTHX. Both outlet temperatures correspond to the secondary streams, transferring heat from and to the HTHP's primary cycle as shown in Fig. 2. The chosen set of independent variables consists of four factors and remains unchanged among all three objective values. It should be noted, the inlet mass flow $\dot{m}_{\mathrm{III}}$ of the LTHX is assumed to be constant and is thus not considered as factor. Each factor is varied over five factor levels and within a certain range enclosed by their respective lowest and highest level. The Table 5 provides an overview of the factors and their factor levels.

Subsequently, a full factorial design is chosen to create the three surrogate models. The full factorial design requires simulations at all

Table 5
The chosen factors, factor levels and boundaries. The factors of the surrogate models are the following: inlet temperature T_{I} and inlet mass flow $\dot{m}_{\mathrm{I}}$ of HTHX, inlet temperature T_{III} of LTHX, rotational shaft speed N.

Factors	Factor levels				
	−1	−0.5	0	0.5	1
T_{I} [°C]	177	195.25	213.5	231.75	250
T_{III} [°C]	60	70	80	90	100
$\dot{m}_{\mathrm{I}}$ [kg/s]	5	7.75	10.5	13.25	16
N [–]	0.8	0.9825	1.165	1.3475	1.53

Table 6
The three resulting surrogate models created to describe the HTHP's functionality. The surrogate models and their regression coefficients are listed in the Appendix C.

Factors	Polynomial degree	R^2
P_{HTHP} [kW]	2nd	99.9105
T_{II} [°C]	3rd	99.9423
T_{IV} [°C]	2nd	98.8331

possible factor level-combinations, which amounts to $5^4 = 625$ simulations. Based on the Ebsilon simulations of the HTHP, three surrogate models are created.

There are various approaches for the construction of surrogate models such as model types based on polynomial regression, Kriging, radial basis functions or neural networks [63,67]. One of the most commonly used technique are polynomial surrogate models, which are computationally cheap to construct and are well-suited to low-dimensional, nonlinear problems. For details on polynomial surrogate models the reader is referred to text books, e.g. [68].

The model function from which the surrogate models are derived consists of a 2nd or 3rd degree polynomial with the general form:

$$F(\boldsymbol{x}, \boldsymbol{\alpha}) = \sum_{i=0}^{d} \sum_{j=0}^{d-i} \sum_{k=0}^{d-i-j} \sum_{l=0}^{d-i-j-k} \alpha_{ijkl} x_1^i x_2^j x_3^k x_4^l \tag{4}$$

with regression coefficients $\boldsymbol{\alpha} = \alpha_{ijkl}$ and for which the variables $\boldsymbol{x} = (x_1, x_2, x_3, x_4)$ correspond to the factors $\boldsymbol{x} = (T_{\mathrm{I}}, \dot{m}_{\mathrm{I}}, T_{\mathrm{III}}, N)$.

The decision whether terms in (4) are significant and therefore, have to be included in the respective surrogate model is made with an analysis of variance (ANOVA). In general, each term describes the influence one factor or a combination thereof has on the objective value. Statgraphics XIX [69] is used to conduct the ANOVA based on the simulation results. The confidence interval is set to 95% and all insignificant terms (p-values ≥ 0.05) were removed from the respective general function (4). Subsequently, regression coefficients were calculated by multi-linear-regression yielding the three surrogate models. The coefficient of determination R^2 served as a measure to describe the quality of the fit. Among the three objective values, T_{II} has a high impact on the transferred heat flow rates, consequently high R^2 values are a requirement. Therefore, a 3rd degree polynomial is chosen for T_{II} to increase R^2 to $\geq 99.9\%$. As for P_{HTHP}, the 2nd degree polynomial already fulfilled this requirement. Table 6 provides an overview over the polynomial degrees and R^2 values.

With all R^2 values above 98.8%, the three surrogate models describe with high accuracy how the electrical power and the two outlet temperatures of the HTF and the waste heat air stream depend on the four operational parameters (cf. Table 6).

3.1.2. Steam generator surrogate model

The energy balance in Eq. (5) serves as the basis for the derivation of algebraic equations modeling the thermal performance of the steam generator:

$$T_{\mathrm{out}} = T_{\mathrm{in}} - \frac{\dot{Q}}{\dot{m} c_{\mathrm{p,f}}} \tag{5}$$

where: T_{out} : outlet HTF temperature in °C
T_{in} : inlet HTF temperature in °C
$\dot{m}$: HTF mass flow rate in kg/s
$c_{\mathrm{p,f}}$: heat capacity of HTF

As described in Section 2.2, a data set of steady-state operating points is calculated using Ebsilon. The resulting data set provides the required input to estimate the function parameters of the following equations:

$$T_{\mathrm{out}} = \alpha_0 + \frac{\alpha_1}{\dot{m}} \tag{6}$$

$$T_{\mathrm{in}} = \beta_0 + \frac{\beta_1}{\dot{m}} \tag{7}$$

using a least squares error method. The solution yields the following coefficients:

$$T_{\mathrm{out}} = 196.3 - \frac{188.4}{\dot{m}} \tag{8}$$

$$T_{\mathrm{in}} = 201.92 + \frac{1819.32}{\dot{m}} \tag{9}$$

3.2. Mathematical formulation

To compute the optimal operation of the proposed system, a nonlinear optimization problem has to be formulated based on the described component models. Consequently, the optimization problem has to be solved, which is formulated by three blocks: objective function, system constraints and technical restrictions.

3.2.1. Objective function

This research focuses on single-objective optimization, more precisely on a cost- or emission-optimal operation. Therefore the aim is to minimize the operating costs or indirect emissions related to the consumed grid electricity.

The general objective function of the optimization problem can be formulated over a continuous operating horizon $[0, t_f]$ as follows:

$$J(P_{\mathrm{grid}}) = \int_0^{t_f} C\left(P_{\mathrm{grid}}(t)\right) \mathrm{d}t \tag{10}$$

Here, J represents either the operating costs or the CO_2 emissions using

$$C\left(P_{\mathrm{grid}}(t)\right) = P_{\mathrm{grid}}(t) g_{\mathrm{pr,grid}}(t) \tag{11}$$

$$C\left(P_{\mathrm{grid}}(t)\right) = P_{\mathrm{grid}}(t) g_{\mathrm{em,grid}}(t) \tag{12}$$

where $g_{\mathrm{pr,grid}}(t)$ is the electricity price, $g_{\mathrm{em,grid}}(t)$ are the CO_2 emissions of the electricity grid and $P_{\mathrm{grid}}(t)$ is the electrical energy consumed from the grid at time t. The input data $g_{\mathrm{pr,grid}}(t)$ and $g_{\mathrm{em,grid}}(t)$ are provided by the ENTSO-E TP, cf. Section 2.5.

3.2.2. System constraints

The objective function is subject to different constraints resulting from physical laws such as power and heat flow rate equations of the system components and their interconnection, as illustrated in the proposed structure in Fig. 6.

High temperature heat pump. According to the proposed system structure, the power balance and outlet temperature equations, which describe the HTHP part-load behavior in detail, can be stated as follows:

$$F_{\mathrm{HTHP}}\left(T_{\mathrm{I}}(t), \dot{m}_{\mathrm{I}}(t), T_{\mathrm{III}}(t), N(t)\right) = P_{\mathrm{grid}}(t) + P_{\mathrm{wt}}(t) \tag{13}$$

$$F_{\mathrm{HTHX}}\left(T_{\mathrm{I}}(t), \dot{m}_{\mathrm{I}}(t), T_{\mathrm{III}}(t), N(t)\right) = T_{\mathrm{II}}(t) \tag{14}$$

$$F_{\mathrm{LTHX}}\left(T_{\mathrm{I}}(t), \dot{m}_{\mathrm{I}}(t), T_{\mathrm{III}}(t), N(t)\right) = T_{\mathrm{IV}}(t) \tag{15}$$

where $F_{\mathrm{HTHP}}, F_{\mathrm{HTHX}}$ and F_{LTHX} represent the polynomial surrogate models (4) for electrical power, outlet oil and air temperature, respectively. As mentioned, selling the wind turbine power P_{wt} to the grid is not allowed. The balance Eq. (13) therefore implies that renewable electricity that is not completely consumed by steam generation, within

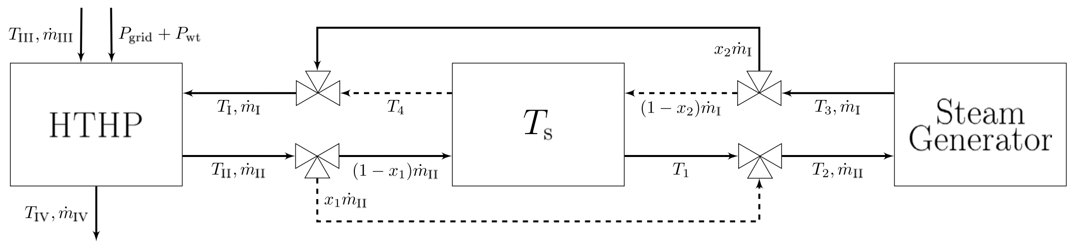

Fig. 6. Schematic flow diagram of the regenerative steam generation including HTHP, TES and steam generator. The HTHP and the steam generator are represented by a polynomial surrogate model, while the TES is modeled by an effectiveness model, see Sections 3.1 and 2.3. A controllable fluid bypass $x_1 \in [0,1]$ is used to control the heat supply to the TES. Conversely, bypass $x_2 \in [0,1]$ regulates the heat supplied by the HTHP depending on the thermal state T_s of the TES. In addition, the *solid* and *dashed* lines indicate the charging and discharging mode, respectively, in a simplified manner. In the proposed setup, charging and discharging at the same time is not allowed. For instance, in the *charge* mode it is $x_1 \in [0,1), x_2 = 1$, the *discharge* mode implies $x_2 \in [0,1), x_1 = 1$.

the same time period, is forced into the storage by increasing the temperature level of the HTHP.

It is assumed that the positive input power P_{grid} possesses no specific operational limits and is thus not restricted by lower and upper bounds. In addition, P_{grid} and $T_{\mathrm{II}}, T_{\mathrm{IV}}$ are limited directly by the capacity of the wind turbine and the selected factor set, respectively. It should also be noted that the mass flow rates within the secondary hot side (cf. Fig. 6) are equal, i.e. $\dot{m}_{\mathrm{I}} = \dot{m}_{\mathrm{II}}$.

Thermal energy storage. The model of the TES was introduced in Section 2.3. The relation between the steady-state transferred heat rate $\dot{Q}_{\mathrm{f}}$ and the storage temperature T_{s} is defined by (3) without considering thermal losses. More specifically, this relation represents an energy balance, describing the change of storage temperature with regard to the current operation of the storage.

$$\frac{\mathrm{d}T_{\mathrm{s}}(t)}{\mathrm{d}t} = \frac{\dot{Q}_{\mathrm{s,ch}}(t) - \dot{Q}_{\mathrm{s,dch}}(t)}{m_{\mathrm{s}} c_{\mathrm{p,s}}} \tag{16}$$

The charge and discharge heat flow rate depend on the HTF mass flow, the temperature level and the fluid flow splitting (cf. Section 2.3.3). Consequently, both can be calculated using fluid bypasses $x_1, x_2 \in [0,1]$ with

$$\dot{Q}_{\mathrm{s,ch}}(t) = \dot{m}_{\mathrm{II}}(t) c_{\mathrm{p,f}} \big(T_{\mathrm{II}}(t) - T_1(t)\big)\big(1 - x_1(t)\big) \tag{17}$$

$$\dot{Q}_{\mathrm{s,dch}}(t) = \dot{m}_{\mathrm{I}}(t) c_{\mathrm{p,f}} \big(T_4(t) - T_3(t)\big)\big(1 - x_2(t)\big) \tag{18}$$

The heat transfer rate is inherently interpreted as positive and negative when charging and discharging, respectively. Note, that the temperature difference within (18) is modeled correctly, since the mentioned negative relation is already built into (16).

The outlet temperatures T_1 and T_4 of the TES included in (17)–(18) are determined by the introduced effectiveness model (2) and can be found through

$$T_1(t) = T_{\mathrm{II}}(t) - \epsilon_{\mathrm{ch}} \big(T_{\mathrm{II}}(t) - T_{\mathrm{s}}(t)\big) \tag{19}$$

$$T_4(t) = T_3(t) - \epsilon_{\mathrm{dch}} \big(T_3(t) - T_{\mathrm{s}}(t)\big) \tag{20}$$

where ϵ_{ch} and ϵ_{dch} represents the constant charge and discharge efficiencies.

As a technical constraint, we assume that simultaneous charging and discharging of the TES is not possible. To ensure that the system does not charge and discharge at the same time, the following constraint is applied:

$$\dot{Q}_{\mathrm{s,ch}}(t)\dot{Q}_{\mathrm{s,dch}}(t) = 0 \tag{21}$$

To avoid the complementarity constraint (21), additional binary variables can be introduced, see e.g. [20], that interpret the on/off mode of charging and discharging the TES. However, the resulting mixed integer nonlinear optimization problem is much more challenging to solve numerically. For this reason we deal with (21) and circumvent this difficulty from a computational point of view.

It should be mentioned that limits for the minimum and maximum transferred heat rate exchange are neglected. Furthermore, limitations on the TES capacity are naturally determined by the HTHX outlet and inlet temperatures and the system structure itself.

Steam generator. In order to ensure a constant heat supply by fulfilling the energy balance (5), the required thermal energy is supplied by HTHP and TES in combination with the fluid flow regulation. Therefore, the surrogate-based inlet temperature T_2 of the steam generator must satisfy:

$$T_2(t) = T_{\mathrm{II}}(t)x_1(t) + T_1(t)\big(1 - x_1(t)\big) \tag{22}$$

$$T_2(t) = 201.92 + \frac{1819.32}{\dot{m}_{\mathrm{II}}(t)} \tag{23}$$

Conversely, the required HTHP's thermal energy is controlled by

$$T_{\mathrm{I}}(t) = T_3(t)x_2(t) + T_4(t)\big(1 - x_2(t)\big) \tag{24}$$

$$T_3(t) = 196.3 - \frac{188.4}{\dot{m}_{\mathrm{I}}(t)} \tag{25}$$

with the surrogate-based outlet temperature T_3. Due to the system structure, the temperatures T_2 and T_3 are naturally limited by a lower and upper bound.

Overall, the proposed system structure can easily be understood as follows: in *idle mode* it holds $\dot{Q}_{\mathrm{s,ch}} = \dot{Q}_{\mathrm{s,dch}} = 0$, $x_1 = x_2 = 1$, $T_2 = T_{\mathrm{II}}$ and $T_{\mathrm{I}} = T_3$; in *charging mode* it follows $\dot{Q}_{\mathrm{s,ch}} > 0, \dot{Q}_{\mathrm{s,dch}} = 0$, $x_1 \in [0,1), x_2 = 1$, $T_{\mathrm{I}} = T_3$ and $T_2 = T_{\mathrm{II}}x_1 + T_1(1 - x_1)$; analogous for the *discharging mode*.

3.2.3. Mathematical optimization problem

Finally, the optimization problem (10)–(24) is solved numerically. The direct method is employed for the numerical solution, in which the continuous version is reformulated into a discrete multi-period nonlinear optimization problem by discretizing the time. In this setting, the continuous time axis $[0, t_f]$ is replaced by a discrete domain by $n+1$ uniformly spaced discrete time points with $\Delta t := t_k - t_{k-1}$.

Consequently, the functions are only considered at the discrete time points t_k, i.e. $T_{\mathrm{I}}^k := T_{\mathrm{I}}(t_k)$ for $k = 1, 2, \ldots, n$. In between, the functions are interpolated linearly. The charging/discharging behavior in Eq. (16) is approximated by numerical differentiation as follows:

$$\frac{\mathrm{d}T_{\mathrm{s}}(t_k)}{\mathrm{d}t} \approx \frac{T_{\mathrm{s}}(t_k) - T_{\mathrm{s}}(t_{k-1})}{t_k - t_{k-1}} =: \frac{T_{\mathrm{s}}^k - T_{\mathrm{s}}^{k-1}}{\Delta t} \tag{26}$$

In a similar manner, the objective function is discretized by numerical integration and becomes

$$\int_0^{t_f} C\big(P_{\mathrm{grid}}(t)\big)\,\mathrm{d}t = \sum_{k=1}^{n} C\big(P_{\mathrm{grid}}^k\big)\Delta t \tag{27}$$

Combining everything, the complete optimization problem in discrete setting for $k = 1, 2, \ldots, n$ takes the following form:

$$\min\ J(P_{\mathrm{grid}}) = \sum_{k=1}^{n} C\big(P_{\mathrm{grid}}^k\big)\Delta t \tag{28}$$

subject to Eqs. (13)–(15), (17), (18), (22)–(25) and

$$T_1^k = T_{II}^k - \epsilon_{ch}\left(T_{II}^k - T_s^{k-1}\right) \tag{29}$$

$$T_4^k = T_3^k - \epsilon_{dch}\left(T_3^k - T_s^{k-1}\right) \tag{30}$$

$$T_s^k = T_s^{k-1} + \frac{\dot{Q}_{s,ch}^k - \dot{Q}_{s,dch}^k}{m_s c_{p,s}} \Delta t \tag{31}$$

$$\dot{Q}_{s,ch}^k \dot{Q}_{s,dch}^k \leq \gamma \tag{32}$$

$$T_s^0 = \widetilde{T}_0 \tag{33}$$

$$T_s^n = T_s^0 \tag{34}$$

The complete discretized optimization problem can be found in Appendix D, cf. (38)–(53).

In the Eqs. (29) and (30), which refer to the discretized effectiveness model, the mean storage temperature of the previous period t_{k-1} is used. For a correct setting, an initial storage temperature $\widetilde{T}_0$ must be included. We define that the storage temperature at the end of the operating period is equal to the temperature at the beginning, i.e. $T_s^n = \widetilde{T}_0 = 250\,°\mathrm{C}$. Cyclic boundary conditions are often considered in practice, e.g. [70]. The complementarity constraint (21) leads to difficulties both theoretically and numerically. Therefore, we apply a common constraint relaxation strategy [71] by introducing a relaxation parameter $0 < \gamma \ll 1$ in Eq. (32), which is numerically advisable.

3.2.4. Optimization method

The optimization problem (38)–(53) is deterministic, nonlinear and nonconvex and can be solved in principle with any nonlinear programming (NLP) solver. Based on its nonconvex solution subspace, the problem may have multiple feasible regions and locally optimal points and a unique global optimum cannot be guaranteed [72]. For numerical solution of the underlying optimization problem using NLP solvers, local and global deterministic optimization methods can be used. Local optimization algorithms compute a local optimum that is strongly dependent on the selected starting point. Consequently, the choice of a starting point determines the convergence rate to a solution and to which optimum the algorithm converges. In addition, local methods can perform poorly and even fail if starting points are unfavorably chosen. However, there is a variety of very robust, reliable and highly efficient solvers that are designed to solve large-scale NLP problems. In contrast, global deterministic optimization methods attempt to find the global solution, while ensuring theoretical constraint qualifications within a desired tolerance and can offer a theoretical guarantee of convergence under certain convexity assumptions. Nevertheless, state-of-the-art global optimization solvers, such as BARON [73], lead to intensive computational costs, for which the CPU time required to solve these problems (even for smooth problems) increases rapidly with the number of variables and constraints.

The case study presented in Section 4 considers a 168-h optimal operation task that cannot be solved in a reasonable time using global optimization methods. In order to ensure a high qualitative numerical solution, a local optimization algorithm is used in combination with a multi-start method. The latter means, that the local optimization routine runs repeatedly from various different initialization points to capture a large variety of locally optimal solutions, from which the one with the best objective value is then saved as the proposed global solution. However, there is no guarantee in determining the global minimum.

Let us mention that it is also possible to linearize the original nonlinear optimization problem using standard linearization techniques. In this context, suitable linearization methods are to be applied to the bilinear terms (42)–(43), the trilinear terms (46)–(47) (transformed first into bilinear terms), the nonlinear terms (44)–(45) and the nonlinear polynomial surrogate models (39)–(41). However, we do not explicitly perform a linearization here.

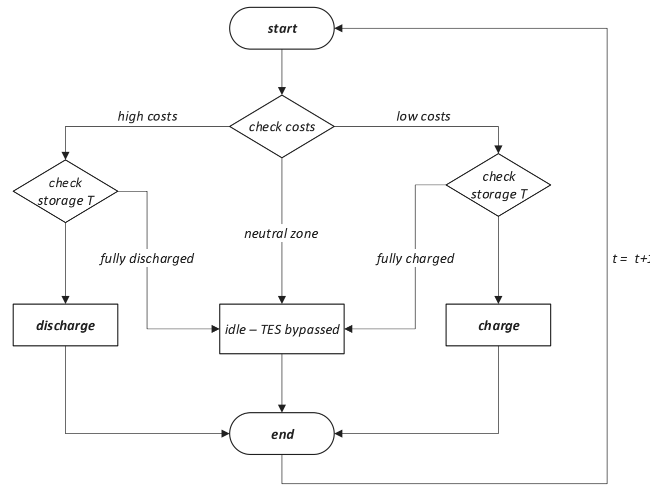

Fig. 7. Decision flow chart of the problem-specific rule-based control strategy. The decisions are divided in the three main operating modes: charge, discharge and idle. Based on the current cost of electricity and consequently the state of charge, an operating mode is selected.

3.3. Rule-based control strategy

In order to investigate the effects of optimal operation, a simple and problem-specific rule-based control strategy is introduced to create a comparable case, where the identical energy system is operated based on momentary data (see Section 2). A rule-based control strategy is an alternative to an optimization-based control. To be more precise, while optimization-based approaches are formulated as optimization problems, rule-based methods use decisions for the cost- or emission-optimal operation that are made on the basis of previously defined rules and regularities. In general, rule-based strategies are often used for the operation of vehicles, production or other complex systems. However, such problem-specific strategies are also used, when considering energy systems, including energy storage technologies, see e.g. [74–76].

As shown in Fig. 7 charging and discharging rates are determined by a series of if-else decisions, which consider the instantaneous input of electricity costs, wind speed and storage temperature. Decisions are based on threshold values to distinguish between charging, discharging and idle state. Each state is set to predefined operating points and oil mass flow. Additional adjustment routines for control parameters are included to prevent violation of system boundaries (e.g. bypass values) and use the available wind energy as feeding electricity to the grid is not allowed. The use of such control strategies enables real-time control, but information about future profiles for costs and availability of renewable energy, which have a strong influence on low-cost or low-emission operation, are not known and thus, not included in the decisions.

In contrast, the optimizer is able to take the inputs of the entire time period into account, to tune the control parameters for each time step, as described in Section 3.2. The output of the control strategy is compared to the results of the optimization-based control to demonstrate differences in the operational strategy and to emphasize the effects of optimization.

4. Results

In this section, we demonstrate and analyze the optimal operation of the proposed multi-component system (cf. Fig. 1) as a potential option for the electrification of high temperature process heat and improvement of its performance. For this reason, we investigate the interaction between the system, the external electricity and wind power over a middle-term operation period. More precisely, the operation

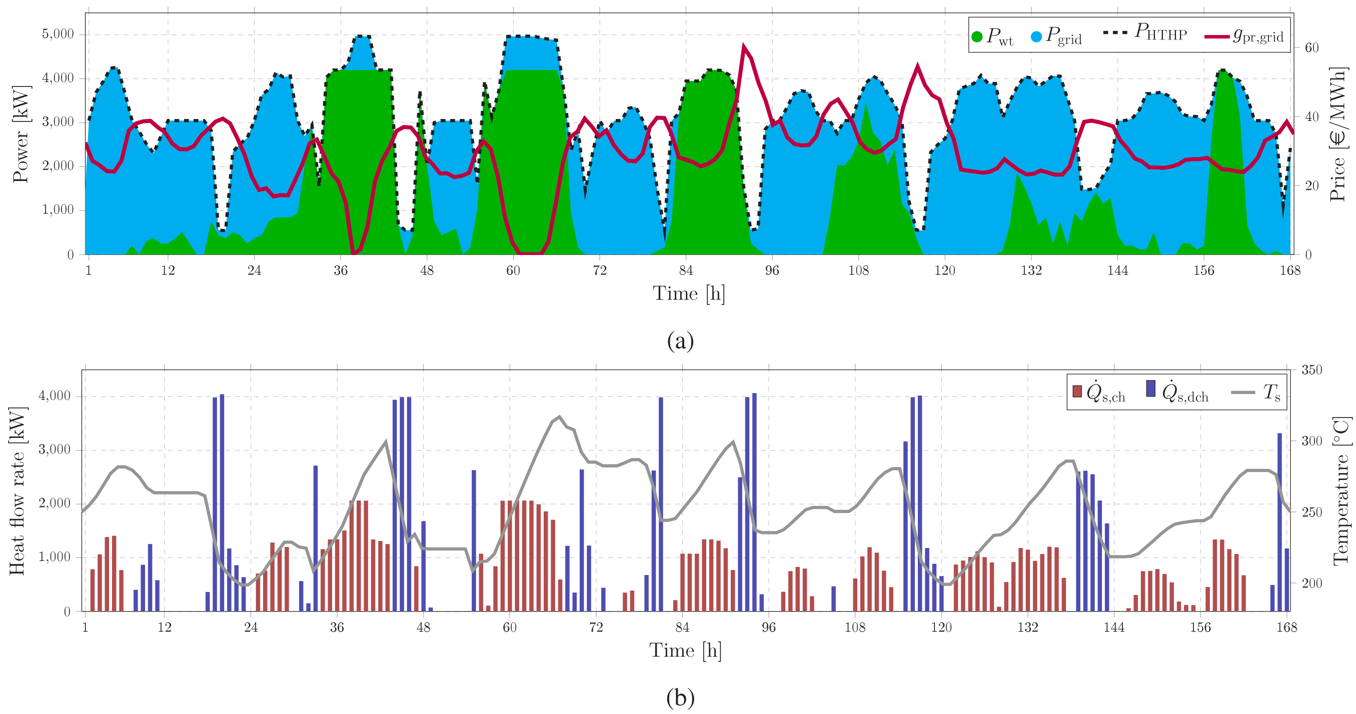

Fig. 8. Visualization of the results of the reference week while minimizing operating cost. (a): Electrical power mix consumption (P_{wt} and P_{grid} are stacked to P_{HTHP}) to operate HTHP and the respective electricity price $g_{pr,grid}$. (b): Transferred heat rates $\dot{Q}_{s,ch}$, $\dot{Q}_{s,dch}$ and storage temperature T_s of the TES.

in one week with 168 discrete time steps Δt of an hour, i.e. n = 168 and Δt = 3600s. The results obtained from the optimization serve as benchmark solution for the development and evaluation of online optimization methods, which do not have access to data without uncertainties of future prices and weather. The input data for the optimization are assumed to be known a priori. Thus, we conduct an offline optimization.

The underlying case study of the 168-h optimal operation task has around 3000 decision variables as well as 2500 constraints and is solved using the popular open-source NLP solver IPOPT [37,77] with 1000 randomly distributed starting points for which the best local optimum is returned in the GAMS environment. Of course, other algebraic optimization modeling languages like the open-source Pyomo library are also easily applicable. Computations are performed with an Intel(R) Core(TM) i7-8665U CPU, with an average CPU time less than 5 min per starting point.

Note that although the waste heat is considered as an independent variable in the surrogate models generated, we assume that this quantity is constant. If not specified otherwise, the available waste heat is fixed to $T_{III} = 75\,°C$ and $\dot{m}_{III} = 5\,\frac{kg}{s}$.

4.1. Optimal operation of reference week

The case study outlined above and the resulting optimization problem were solved for the selected reference week with the given input dataset. The formulated problem was optimized separately in order to minimize either the operating costs or the carbon emissions, which are represented by the introduced objectives (11) and (12), respectively.

Figs. 8 and 9 exemplary show characteristics of several quantities of the cost-optimized operation throughout the selected week. The optimized mix of electrical energy sources and the corresponding overall power consumption together with the electricity price profile is illustrated in Fig. 8(a). For the reference week, the HTHP consumed a total of 535.67 MWh, while 218.34 MWh and 317.33 MWh were provided by wind and grid power, respectively. As defined by the multi-component system, the overall power consumption – represented by the dashed line of the stacked graph – depends on the operation of the storage. Fig. 8(b) visualized the state of charge in terms of the storage temperature T_s and the heat rates transferred to $\dot{Q}_{s,ch}$ or from $\dot{Q}_{s,dch}$ the TES. In addition, the corresponding outlet air temperature T_{IV} of the LTHX is shown in Fig. 9.

The mix between the electrical power consumed (cf. Fig. 8(a)) from the grid and the wind turbine depends mainly on three factors: the electricity price, the currently available wind power and the state of charge of the TES. It is trivial that in an optimal operation, the available wind power is always consumed first, as it can be used without incurring any costs. In times of high prices, a large part of the required amount of heat is provided by the TES, so that the HTHPs have to supply less heat and thus additional costs for grid purchase are minimized. Conversely, during periods of low prices and/or high wind power generation, the TES is heated by the HTHPs to store energy, in which additional and cheaper electrical grid power is usually purchased and used to operate the HTHPs at higher temperature levels. In particular, a correlation between lower electricity prices and times of high wind power can be seen within the reference week. The simultaneous occurrence of high wind power and low electricity prices presents a strong incentive to operate the HTHP at maximum capacity and charge the TES.

Fig. 8(b) shows at hours e.g. 18, 46, 80, 94, 118, 140 and 167 that the electricity price peaks can be successfully avoided by discharging the TES. Compared to the charging process, the discharging process occurs at high heat transfer rates and is thus performed faster. Consequently, the storage temperature drops significantly. The magnitude of charging and discharging rates is partly determined by the energy systems configuration.

The charging rate is limited by the constraint, that the temperature of the HTF T_{II} has to be higher than the current storage temperature T_s. If the temperature of the HTF is too close to the temperature of the TES, the optimizer has to either increase the power supplied to the heat pump and thus increase its thermal output, or if the HTHPs is at peak load, it will reduce the HTF mass flow to reach higher temperatures at the storage inlet T_{II}. Furthermore, the charging rate is limited by the constant heat demand of the steam generator.

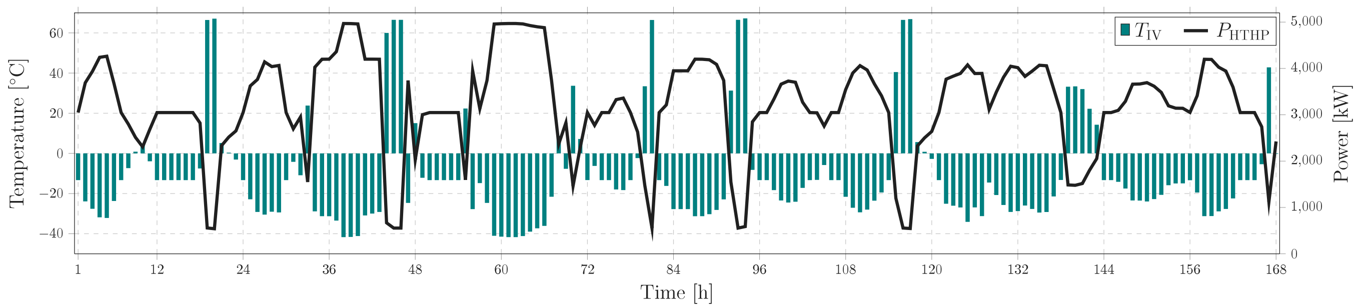

Fig. 9. HTHP electrical power consumption P_{HTHP} and outlet air temperature T_{IV} of the LTHX.

The discharge heat flow rate is higher, because it is not as constrained by the system. The discharging heat flow rate is only limited by the minimum power consumption of the HTHPs, which is about 560 kW electric and the maximum temperature difference between the inlet and outlet of the storage.

A part of the optimization is to decide, whether it is economically viable to buy additional electricity to charge the TES faster or to use only the wind power. Charging the TES faster would imply buying grid electricity and operating the HTHPs at higher load and thus less efficiently.

It should also be mentioned that very short charge or discharge cycles such as at hour 73, 75 and 104 are probably not achievable in reality. Hoivik [51] operated a TES with cycle times of 5 or more hours. The inertia of the components is not considered here, but can be integrated into the optimization problem with additional constraints.

Moreover, the results indicate that the storage capacity appears to be appropriate, due to the timescale in which the electricity prices peak. The TES is able to provide enough heat to circumvent extended periods of expensive grid power. The trade-off between the beneficial effect of a larger TES and the related increase in investment cost has to be investigated. A techno-economic analysis is not conducted in this paper and is subject to future work.

As already emphasized, in addition to high temperature process heat, process cooling is also generated by the Brayton process, illustrated in Fig. 9. According to the current state of the design, temperatures significantly below 0 °C can be reached on heat source exit. Temperatures of approximately −13 °C and up to −42 °C are reached in idle and charging mode. During discharging, the heat pump operates at lower pressure ratios and thus lower temperature levels, so less waste heat is absorbed at the heat source. Therefore, the outlet air temperature T_{IV} can reach up to 66 °C in discharge mode. The utilization of the cold temperatures at the LTHX outlet to cover industrial cooling demand or to supply a cold storage will be addressed in future work.

Fig. 10 shows the comparison of the temporal process of the storage temperatures $T_{\mathrm{s,co}}$ and $T_{\mathrm{s,em}}$ for a cost- and emission-optimized system, respectively. Although the emission factor of the electricity generation mix $g_{\mathrm{em,grid}}$ represents a very similar overall trend to the electricity price $g_{\mathrm{pr,grid}}$ (cf. Fig. 8), significant differences in system operation can be observed at certain time steps:

- In the first 24 h, emission factors are high and wind power is low, so for emission-optimized operation the storage is discharged immediately.
- In time period 96–120 h, charging and discharging is timed differently to compensate for high emission factors and low wind speeds.
- From 138 h to 168 h, emission minimization leads to slower discharge and charge rates, as grid emissions are at a high level.

The similarities addressed are to be expected, since there is a strong dependency on the wind turbine power, which is considered to be emission and cost neutral. However, with the discussed study, it can be shown that both objectives should be considered for optimal operation of future energy systems to select the best trade-off between costs and emissions from a Pareto front. All calculated solutions and their respective objective values for both optimization tasks can be found in Appendix E.

Table 7
The objective value of the reference week obtained **with and without** the use of the TES by minimizing **operating costs** [€], assuming different constant waste heat levels T_{III}.

T_{III} [°C]	With TES [€]	Without TES [€]
60	12,245.44	13,521.59
75	11,835.42	13,169.85
90	11,453.97	12,823.1

Table 8
The objective value of the reference week obtained **with and without** the use of the TES by minimizing CO_2 emissions [t], assuming different constant waste heat levels T_{III}.

T_{III} [°C]	With TES [t]	Without TES [t]
60	105.34	115.36
75	101.01	111.73
90	97.01	108.15

Finally, Tables 7 and 8 present the objective values for cost- and emission-optimized operation with and without the use of the TES component at different heat source levels. Increasing the heat source temperature has an inherently positive effect on both operating costs and emissions. A higher heat source temperature leads to a lower temperature lift and thus to a better COP. Subsequently, the same amount of heat can be provided with lower power consumption. This effect is directly reflected in the objective values by a reduction in costs and emissions with and without TES of about 4% and 3%, respectively, at a 15 °C higher source temperature. As expected, the multi-component system with TES offers the advantage that excess energy is stored when high wind power and/or low electricity prices (emission factors) are available and is used to reduce the electricity consumption at peak electricity prices (emission factors). Depending on the temperature level of the waste heat, the operating costs without TES are 13%–15% higher. Similarly, the emission-optimized operation causes – also depending on the heat source temperature level – about 9 to 11% higher CO_2 emissions if the system does not include a thermal storage.

4.2. Optimized versus rule-based operation

By using a control of the system based on an offline optimized control, electricity prices and wind power can be taken into account over the entire period, so that charging and discharging rates are optimally set in terms of magnitude and time to save the maximum amount of energy costs. To evaluate the performance of this approach, a simple and problem-specific rule-based control strategy (cf. Section 3.3) is used for comparison. In the following, the reference week is analyzed with

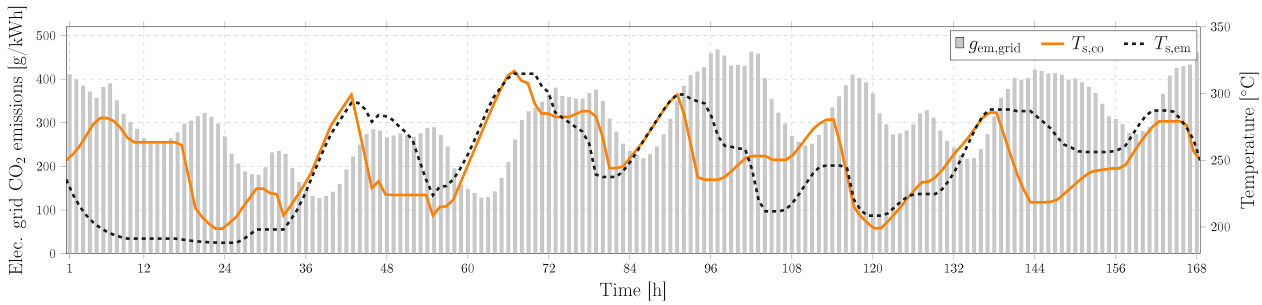

Fig. 10. Visualization of the results of the reference week with regard to minimizing operating costs or CO_2 emissions. The stored heat $T_{s,co}$ and $T_{s,em}$ associated to the optimization problem of minimizing costs or emissions, respectively, is compared. In addition, the respective CO_2 emission factor of power generation mix $g_{em,grid}$ is illustrated.

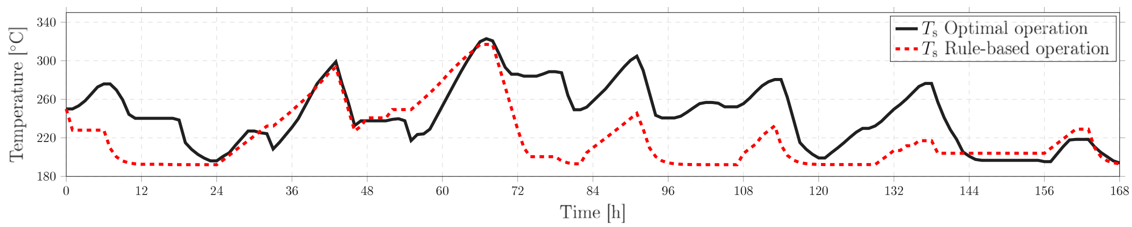

Fig. 11. Result of the reference week while minimizing operating cost between optimal and rule-based operation for T_s. We note that the final storage temperature is not specified at the end of the optimization period, as this aspect is not taken into account in the rule-based control strategy.

the proposed rule-based control scheme shown in Fig. 7. In doing so, the result of the optimization-based control, which represents the most efficient way to operate the energy system under the given boundary conditions, is used as a benchmark.

As explained earlier, the simplified control strategy determines the charging and discharging rates based only on the instantaneous input data at time t. Fig. 11 shows the temporal course of the storage temperature for both control schemes. It can be seen that the overall trend in charging and discharging is similar for most of the week. The amount of energy stored e.g. at hours 24, 48, 68 or 160 matches for both strategies. But as expected, there are some significant differences:

- The discharging processes at hours 18, 30, 55, 78 and 138 determined by the optimization are not reflected by the rule-based operation.
- Opposite trends can be seen at the beginning of the week, as the rule-based control strategy discharges the storage during the first 12 h.
- For decisions based only on momentary input, the TES is discharged as soon as the energy costs fall below the threshold value.

Exact knowledge about future prices and weather, as assumed in the offline optimization, allows for significant reduction of operating costs, as shown in Table 9. In contrast, the rule-based control strategy deviates from the optimum by approximately 6.04%. However, the solution can be computed in real-time as the simplified scheme is based only on if-else statements.

One of the goals of future research is to apply methods that get as close as possible to the optimal solution while maintaining real-time, online capability.

4.3. Impact of seasonality on the weekly operation

Lastly, we compare different scenarios of available wind energy and emission factors throughout the year. However, the optimization problem of the 8784-h system operation for an entire year possesses around 158000 variables and 140000 constraints, whereby the CPU time requires several days per starting point when using the IPOPT solver. To circumvent the computational burden associated with employing a multi-start approach for an entire year featuring a substantial number of starting points, this study aims to optimize individual weeks within each month independently. The proposed methodology enables the derivation of reliable estimates concerning both seasonality's effects and the savings by optimal operational for the entire year, without compromising the dependability of the results by incorporating the multi-start approach.

Table 9
Comparison of best objective value of the reference week obtained while minimizing the **operating costs** between **optimal operation** and the **rule-based control strategy**, assuming a constant waste heat T_{III} = 75 °C.

Method	Operating costs [€]
Optimal operation	11,673
Rule-based strategy	12,378
Relative difference	6.04%

By summing the emissions and cost over the optimally operated weeks of each month, a monthly value can be derived. In Table 10 the resulting values for emissions and cost can be found. Fig. 12 demonstrates the connection between the overall operating cost c_{sys}, the grid electricity price $g_{pr,grid}$ and the generated wind power P_{wt}. From February to May, the grid electricity prices are relatively low, the wind power generation is considerably high and consequently the overall operating cost are low. However, throughout June to September rising grid electricity prices have a direct impact and lead to rising operating cost.

A similar trend can be seen for the emission-optimized weeks in Fig. 13. In times of low wind power generation and high grid emission factors, the system consequently emits higher masses of CO_2. As already pointed out in Fig. 5, a correlation between higher grid electricity prices and grid emission factor exists. Thus, the results for minimized emissions and minimized operating cost behave similarly.

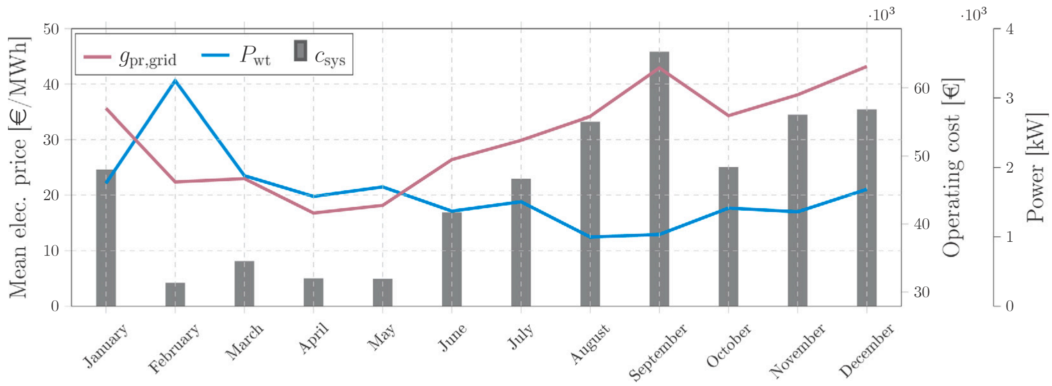

Fig. 12. Results of the individually optimized weeks minimizing the operating cost. The monthly values represent the sum of the objective values of the individual weeks. Furthermore, the electricity price $g_{pr,grid}$ and the wind power P_{wt} are visualized.

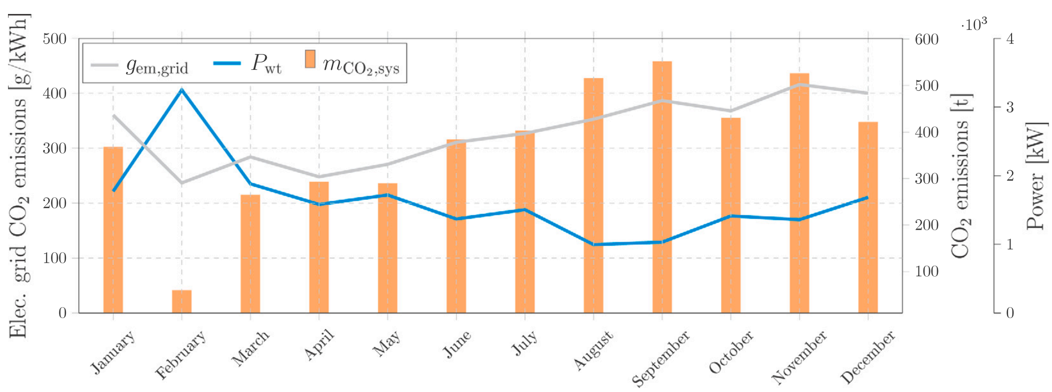

Fig. 13. Results of the individually optimized weeks minimizing the CO_2 emissions. The monthly values represent the sum of the objective values of the individual weeks. Furthermore, the electricity price $g_{em,grid}$ and the wind power P_{wt} are visualized.

Table 10
The objective values by minimizing operating cost and CO_2 emissions on a weekly basis. The monthly values represent the sum of the objective values of the individual weeks.

Month	Operating costs [€]	CO_2 emissions [t]
January	48,021.68	368.3
February	31,343.2	60.1
March	34,531.5	264.7
April	32,022.4	293.2
May	31,931.8	289.5
June	41,702.1	384.3
July	46,637	403.1
August	55,051.4	515.9
September	65,306.4	552.17
October	48,378.3	430.2
November	56,050.4	526.3
December	56,829.3	421.5

5. Conclusion

This study presents a detailed approach to model and optimize the operation of a heat pump based power to heat system supported by a TES and a wind turbine. By means of polynomial surrogate models, the method takes part-load behavior of the components into account. Aiming for optimal control, the large scale optimization problem is solved with a multi-start IPOPT solver to minimize costs or emissions for a time period of one week, to compensate fluctuating wind conditions and variable electricity prices.

The results have shown that offline optimization-based operation, assuming full knowledge of inputs over the entire analyzed period, is able to exploit the benefits and avoid the drawbacks of time-dependent fluctuations in availability of renewable energy, electricity prices and the grid emissions. To put the results into context, a rule-based control strategy serves as a comparison case. The optimized operation causes approximately 6% less operational costs. The results underline the importance to gain knowledge over the time-dependent inputs as accurately as possible.

Some aspects of operational optimization, such as dynamic behavior during load shifts and uncertainties in input data, have not been considered. However, these limitations give inspiration for future work. In real-world scenarios, the optimization problem is affected by uncertainties in energy prices, emissions and weather forecasts. As a consequence, the formulated conceptual problem would be inaccurate and the system state will not evolve as predicted. To overcome this problem robust optimization, stochastic optimization or a model predictive control framework can be applied. On this basis, two future research topics are essential: the precise prediction of input variables and time-efficient, global optimization methods.

CRediT authorship contribution statement

Jasper V.M. Walden: Conceptualization, Methodology, Validation, Resources, Visualization, Data curation, Writing & reviewing. **Martin**

Bähr: Software, Validation, Formal analysis, Investigation, Visualization, Writing & reviewing. **Anselm Glade:** Conceptualization, Methodology, Validation, Writing & reviewing. **Jens Gollasch:** Conceptualization, Methodology, Resources, Writing & reviewing. **A. Phong Tran:** Conceptualization, Methodology, Resources, Writing & reviewing. **Tom Lorenz:** Conceptualization, Formal analysis, Writing, Supervision.

Declaration of competing interest

The authors declare that they have no known competing financial interests or personal relationships that could have appeared to influence the work reported in this paper.

Data availability

Data will be made available on request.

Acknowledgments

The authors declare no competing interests. This research did not receive any specific grant from funding agencies in the public, commercial, or not-for-profit sectors.

Appendix

Supplementary data on this article are given below.

Appendix A. High temperature heat pump model

Corresponding to the thermodynamic cycle shown in Fig. 2 based on the HTHP used, the associated $T-s$ diagram is shown in Fig. A.1.

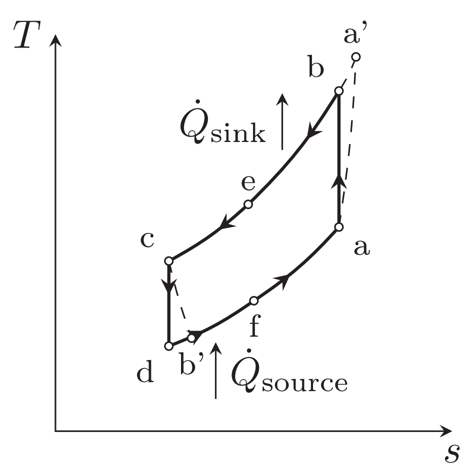

Fig. A.1. Temperature-entropy diagram of the recuperated reverse Brayton cycle.

Appendix B. Thermal energy storage

Analogous to the verification of the charging process of the heat storage module, the discharging process was simulated as shown in Fig. B.1 with the effectiveness model and the parameters specified in Table 3. The storage is cooled from an initial temperature of 350 °C with an HTF temperature of 200 °C. Similar to Fig. 4, the characteristics of the discharging process are correctly modeled while minor errors occur.

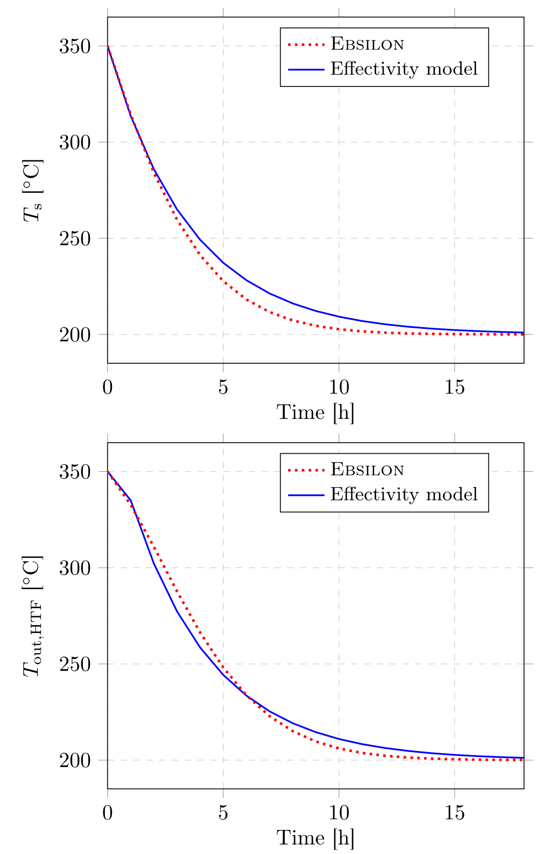

Fig. B.1. Storage temperature and HTF outlet temperature during the discharging process. The parameters involved in the verification simulation are shown in Table 3.

Furthermore, in addition to the Table 4 showing the error metrics of the model, the parity plot for the TES model is presented in Fig. B.2.

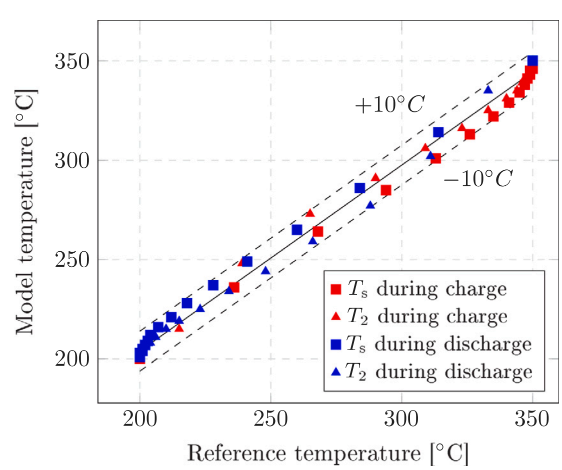

Fig. B.2. Parity plot for temperature deviations between the effectivity model and the EBSILON reference simulation during charging (red) and discharging (blue). The black line indicates values for no deviations.

Appendix C. Surrogate models

As mentioned in Section 3.1.1, a full factorial design based on 4 factors and 5 factor levels is used to create the surrogate models of the HTHP.

The generated polynomial surrogate models corresponding to the electrical power P_{HTHP} consumed, the outlet oil temperature T_{II} of the HTHX and the outlet air temperature T_{IV} of LTHX are given by:

$$\begin{aligned} P_{\mathrm{HTHP}} = {} & 127.87 + 2.06342 \cdot T_{\mathrm{I}} + 2.55723 \cdot \dot{m}_{\mathrm{I}} + 0.756419 \cdot T_{\mathrm{III}} \\ & - 1164.84 \cdot N - 0.0168942 \cdot T_{\mathrm{I}} \cdot \dot{m}_{\mathrm{I}} \\ & - 2.60579 \cdot T_{\mathrm{I}} \cdot N - 0.540713 \cdot \dot{m}_{\mathrm{I}}^2 + 13.3204 \cdot \dot{m}_{\mathrm{I}} \cdot N \\ & - 1.3829 \cdot T_{\mathrm{III}} \cdot N + 1556.66 \cdot N^2 \end{aligned} \tag{35}$$

$$\begin{aligned} T_{\mathrm{II}} = {} & 95.9612 + 0.93433 \cdot T_{\mathrm{I}} - 0.327753 \cdot \dot{m}_{\mathrm{I}} + 0.0146542 \cdot T_{\mathrm{III}} \\ & - 271.354 \cdot N + 0.00104853 \cdot T_{\mathrm{I}}^2 \\ & + 0.0211819 \cdot T_{\mathrm{I}} \cdot \dot{m}_{\mathrm{I}} - 0.706122 \cdot T_{\mathrm{I}} \cdot N + 1.04924 \cdot \dot{m}_{\mathrm{I}}^2 \\ & - 0.00388073 \cdot \dot{m}_{\mathrm{I}} \cdot T_{\mathrm{III}} - 29.4801 \cdot \dot{m}_{\mathrm{I}} \cdot N \\ & + 0.0595068 \cdot T_{\mathrm{III}} \cdot N + 562.428 \cdot N^2 \\ & - 0.000716825 \cdot T_{\mathrm{I}}^2 \cdot N - 0.00148575 \cdot T_{\mathrm{I}} \cdot \dot{m}_{\mathrm{I}}^2 \\ & + 0.0229386 \cdot T_{\mathrm{I}} \cdot \dot{m}_{\mathrm{I}} \cdot N + 0.203578 \cdot T_{\mathrm{I}} \cdot N^2 \\ & - 0.0405702 \cdot \dot{m}_{\mathrm{I}}^3 + 0.881391 \cdot \dot{m}_{\mathrm{I}}^2 \cdot N \\ & - 2.18172 \cdot \dot{m}_{\mathrm{I}} \cdot N^2 - 151.476 \cdot N^3 \end{aligned} \tag{36}$$

$$\begin{aligned} T_{\mathrm{IV}} = {} & 93.3958 - 0.00692483 \cdot T_{\mathrm{I}} - 0.770173 \cdot \dot{m}_{\mathrm{I}} + 1.30277 \cdot T_{\mathrm{III}} \\ & - 183.866 \cdot N + 0.00313225 \cdot T_{\mathrm{I}} \cdot \dot{m}_{\mathrm{I}} \\ & + 0.234082 \cdot T_{\mathrm{I}} \cdot N + 0.106964 \cdot \dot{m}_{\mathrm{I}}^2 - 2.34999 \cdot \dot{m}_{\mathrm{I}} \cdot N \\ & - 0.555879 \cdot T_{\mathrm{III}} \cdot N + 30.2955 \cdot N^2 \end{aligned} \tag{37}$$

with a 2nd degree polynomial for (35) and (37) as well as a 3rd degree polynomial for (36).

Appendix D. Optimization problem

For completeness, the full optimization problem in discrete setting for $k = 1, 2, \ldots, n$ reads as follows:

$$\min \; J(P_{\mathrm{grid}}) = \sum_{k=1}^{n} C\left(P_{\mathrm{grid}}^k\right) \Delta t \tag{38}$$

subject to:

$$P_{\mathrm{grid}}^k + P_{\mathrm{wt}}^k = 3F_{\mathrm{HTHP}}\left(T_{\mathrm{I}}^k, \dot{m}_{\mathrm{I}}^k, T_{\mathrm{III}}^k, N^k\right) \tag{39}$$

$$T_{\mathrm{II}}^k = F_{\mathrm{HTHX}}\left(T_{\mathrm{I}}^k, \dot{m}_{\mathrm{I}}^k, T_{\mathrm{III}}^k, N^k\right) \tag{40}$$

$$T_{\mathrm{IV}}^k = F_{\mathrm{LTHX}}\left(T_{\mathrm{I}}^k, \dot{m}_{\mathrm{I}}^k, T_{\mathrm{III}}^k, N^k\right) \tag{41}$$

$$T_2^k = T_{\mathrm{II}}^k x_1^k + T_1^k\left(1 - x_1^k\right) \tag{42}$$

$$T_{\mathrm{I}}^k = T_3^k x_2^k + T_4^k\left(1 - x_2^k\right) \tag{43}$$

$$T_2^k = 201.92 + \frac{1819.32}{3\dot{m}_{\mathrm{II}}^k} \tag{44}$$

$$T_3^k = 196.3 - \frac{188.4}{3\dot{m}_{\mathrm{I}}^k} \tag{45}$$

$$\dot{Q}_{\mathrm{s,ch}}^k = 3\dot{m}_{\mathrm{II}}^k c_{\mathrm{p,f}}\left(T_{\mathrm{II}}^k - T_1^k\right)\left(1 - x_1^k\right) \tag{46}$$

$$\dot{Q}_{\mathrm{s,dch}}^k = 3\dot{m}_{\mathrm{I}}^k c_{\mathrm{p,f}}\left(T_4^k - T_3^k\right)\left(1 - x_2^k\right) \tag{47}$$

$$T_1^k = T_{\mathrm{II}}^k - \epsilon_{\mathrm{ch}}\left(T_{\mathrm{II}}^k - T_{\mathrm{s}}^{k-1}\right) \tag{48}$$

$$T_4^k = T_3^k - \epsilon_{\mathrm{dch}}\left(T_3^k - T_{\mathrm{s}}^{k-1}\right) \tag{49}$$

$$T_{\mathrm{s}}^k = T_{\mathrm{s}}^{k-1} + \frac{\dot{Q}_{\mathrm{s,ch}}^k - \dot{Q}_{\mathrm{s,dch}}^k}{m_{\mathrm{s}} c_{\mathrm{p,s}}} \Delta t \tag{50}$$

$$\dot{Q}_{\mathrm{s,ch}}^k \dot{Q}_{\mathrm{s,dch}}^k \leq \gamma \tag{51}$$

$$T_{\mathrm{s}}^0 = \widetilde{T}_0 \tag{52}$$

$$T_{\mathrm{s}}^n = T_{\mathrm{s}}^0 \tag{53}$$

The proposed system is designed so that three HTHPs run in parallel in order to keep their capacity on a moderate scale compared to the pilot plant. This is taken into account in (39) and (44)–(47) by multiplication with the factor 3. Eq. (39) represents three times the amount of electrical power P_{HTHP} consumed, since the surrogate model is derived on the basis of a single HTHP. Furthermore, Eqs. (44)–(47) reflect that the mass flows merge on the hot outlet side of the HTHPs in the secondary cycle.

Appendix E. Objective values for all initialization points

As described in Section 3.2.4, a large set of initialization points have been used to determine an optimum. All local solutions and their respective objective values according to the reference week (cf. Section 4.1) are shown in Fig. E.1. It can be seen that the cost-optimized operation does not simultaneously minimize the corresponding emissions and vice versa. Therefore, multi-objective optimization should be employed in future work to optimize both objectives at the same time.

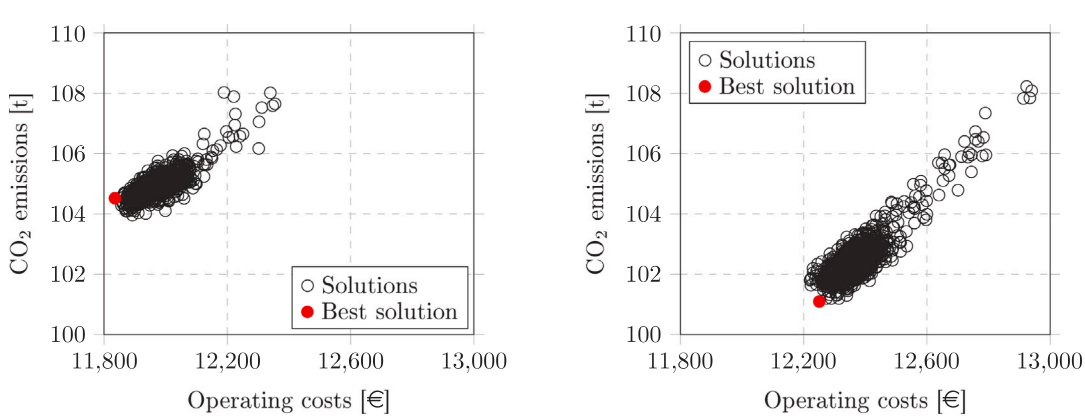

Fig. E.1. Visualization of all objective values, obtained with the IPOPT multi-start approach with 1000 randomly distributed starting points. **(Left):** Solutions based on cost-optimized operation and corresponding CO_2 emissions. **(Right):** Solutions based on emission-optimized operation and corresponding operating costs. The objective values of the best cost- and emission-optimized operation can be found in Tables 7 and 8.

References

[1] Rissman J, Bataille C, Masanet E, Aden N, Morrow WR, Zhou N, et al. Technologies and policies to decarbonize global industry: Review and assessment of mitigation drivers through 2070. Appl Energy 2020;266:114848. http://dx.doi.org/10.1016/j.apenergy.2020.114848.

[2] International Energy Agency, editor. Tracking industrial energy efficiency and CO_2 emissions. Paris; 2007, URL https://www.iea.org/reports/trackingindustrial-energy-efficiency-and-co2-emissions.

[3] Rehfeldt M, Fleiter T, Toro F. A bottom-up estimation of the heating and cooling demand in European industry. Energy Effic 2018;11(5):1057–82. http://dx.doi.org/10.1007/s12053-017-9571-y.

[4] Schüwer D, Schneider C. Electrification of industrial process heat : Long-term applications, potentials and impacts. In: Leading the low-carbon transition : ECEEE industrial summer study ; 11-13 June 2018, Berlin, Germany ; Proceedings. Stockholm: Europ. Council for an Energy Efficient Economy; 2018, p. 411–22, URL http://nbn-resolving.de/urn:nbn:de:bsz:wup4-opus-70377.

[5] Wei M, McMillan CA, de La Rue Can S. Electrification of industry: Potential, challenges and outlook. Curr Sustain/Renew Energy Rep 2019;6(4):140–8. http://dx.doi.org/10.1007/s40518-019-00136-1.

[6] BMWi. Energiedaten: Gesamtausgabe. 2019, URL https://www.bmwi.de/Redaktion/DE/Artikel/Energie/energiedaten-gesamtausgabe.html.

[7] ENTSO-E. Transparency platform. URL https://transparency.entsoe.eu/dashboard/show.

[8] Oehler J, Gollasch J, Tran AP, Nicke E. Part load capability of a high temperature heat pump with reversed Brayton cycle. In: International Energy Agency, editor. 13th IEA heat pump conference 2021 (HPC2020) conference proceedings. 2021.

[9] Oehler J, Tran AP, Stathopoulos P. Simulation of a safe start-up maneuver for a Brayton heat pump. In: Volume 4: Cycle innovations; Cycle innovations: Energy storage. American Society of Mechanical Engineers; 2022, http://dx.doi.org/10.1115/GT2022-79399.

[10] Bühler F, Zühlsdorf B, Nguyen T-V, Elmegaard B. A comparative assessment of electrification strategies for industrial sites: Case of milk powder production. Appl Energy 2019;250:1383–401. http://dx.doi.org/10.1016/j.apenergy.2019.05.071.

[11] Chen C, Lu Y, Banares-Alcantara R. Direct and indirect electrification of chemical industry using methanol production as a case study. Appl Energy 2019;243:71–90. http://dx.doi.org/10.1016/j.apenergy.2019.03.184.

[12] Zhang H, Cai J, Fang K, Zhao F, Sutherland JW. Operational optimization of a grid-connected factory with onsite photovoltaic and battery storage systems. Appl Energy 2017;205:1538–47. http://dx.doi.org/10.1016/j.apenergy.2017.08.140.

[13] Bozchalui MC, Hashmi SA, Hassen H, Canizares CA, Bhattacharya K. Optimal operation of residential energy hubs in smart grids. IEEE Trans Smart Grid 2012;3(4):1755–66. http://dx.doi.org/10.1109/TSG.2012.2212032.

[14] Li J, Ying Y, Lou X, Fan J, Chen Y, Bi D. Integrated energy system optimization based on standardized matrix modeling method. Appl Sci 2018;8(12):2372. http://dx.doi.org/10.3390/app8122372.

[15] Wang C, Lv C, Li P, Song G, Li S, Xu X, et al. Modeling and optimal operation of community integrated energy systems: A case study from China. Appl Energy 2018;230:1242–54. http://dx.doi.org/10.1016/j.apenergy.2018.09.042.

[16] Gambino G, Verrilli F, Canelli M, Russo A, Himanka M, Sasso M, et al. Optimal operation of a district heating power plant with thermal energy storage. In: 2016 American control conference. IEEE; 2016, p. 2334–9. http://dx.doi.org/10.1109/ACC.2016.7525266.

[17] Jing ZX, Jiang XS, Wu QH, Tang WH, Hua B. Modelling and optimal operation of a small-scale integrated energy based district heating and cooling system. Energy 2014;73:399–415. http://dx.doi.org/10.1016/j.energy.2014.06.030.

[18] Geidl M. Integrated modeling and optimization of multi-carrier energy systems (Ph.D. thesis), Zürich: ETH Zürich; 2007, http://dx.doi.org/10.3929/ethz-a-005377890.

[19] Götze J, Dancker J, Wolter M. A general MILP based optimization framework to design energy hubs. At - Automatisierungstechnik 2019;67(11):958–71. http://dx.doi.org/10.1515/auto-2019-0059.

[20] Pazouki S, Haghifam M-R. Optimal planning and scheduling of energy hub in presence of wind, storage and demand response under uncertainty. Int J Electr Power Energy Syst 2016;80:219–39. http://dx.doi.org/10.1016/j.ijepes.2016.01.044.

[21] Ma T, Wu J, Hao L. Energy flow modeling and optimal operation analysis of the micro energy grid based on energy hub. Energy Convers Manage 2017;133:292–306. http://dx.doi.org/10.1016/j.enconman.2016.12.011.

[22] Tian Z, Niu J, Lu Y, He S, Tian X. The improvement of a simulation model for a distributed CCHP system and its influence on optimal operation cost and strategy. Appl Energy 2016;165:430–44. http://dx.doi.org/10.1016/j.apenergy.2015.11.086.

[23] Lu Y, Wang S, Sun Y, Yan C. Optimal scheduling of buildings with energy generation and thermal energy storage under dynamic electricity pricing using mixed-integer nonlinear programming. Appl Energy 2015;147:49–58. http://dx.doi.org/10.1016/j.apenergy.2015.02.060.

[24] Setlhaolo D, Sichilalu S, Zhang J. Residential load management in an energy hub with heat pump water heater. Appl Energy 2017;208:551–60. http://dx.doi.org/10.1016/j.apenergy.2017.09.099.

[25] Sass S, Mitsos A. Optimal operation of dynamic (energy) systems: When are quasi-steady models adequate? Comput Chem Eng 2019;124:133–9. http://dx.doi.org/10.1016/j.compchemeng.2019.02.011.

[26] Cox SJ, Kim D, Cho H, Mago P. Real time optimal control of district cooling system with thermal energy storage using neural networks. Appl Energy 2019;238:466–80. http://dx.doi.org/10.1016/j.apenergy.2019.01.093.

[27] Huang W, Zhang N, Wang Y, Capuder T, Kuzle I, Kang C. Matrix modeling of energy hub with variable energy efficiencies. Int J Electr Power Energy Syst 2020;119:105876. http://dx.doi.org/10.1016/j.ijepes.2020.105876.

[28] Chandan V, Do A-T, Jin B, Jabbari F, Brouwer J, Akrotirianakis I, et al. Modeling and optimization of a combined cooling, heating and power plant system. In: American control conference. 2012, p. 3069–74. http://dx.doi.org/10.1109/ACC.2012.6315606.

[29] Song Y, Hu W, Zhang Z, Hu R, Huang Q, Chen Z. Optimal operation and location of heat pumps in the integrated energy systems. p. 1–6. http://dx.doi.org/10.1109/EI2.2017.8245693.

[30] Ni L, Liu W, Wen F, Xue Y, Dong Z, Zheng Y, et al. Optimal operation of electricity, natural gas and heat systems considering integrated demand responses and diversified storage devices. J Mod Power Syst Clean Energy 2018;6(3):423–37. http://dx.doi.org/10.1007/s40565-017-0360-6.

[31] Lizarraga-Garcia E, Ghobeity A, Totten M, Mitsos A. Optimal operation of a solar-thermal power plant with energy storage and electricity buy-back from grid. Energy 2013;51:61–70. http://dx.doi.org/10.1016/j.energy.2013.01.024.

[32] Si Y, Li X, Yin D, Liu R, Wei J, Huang Y, et al. Evaluating and optimizing the operation of the hydropower system in the Upper Yellow River: A general LINGO-based integrated framework. PLoS One 2018;13(1):e0191483. http://dx.doi.org/10.1371/journal.pone.0191483.

[33] Housh M. Optimization of multi-quality water networks: Can simple optimization heuristics compete with nonlinear solvers? Water 2021;13(16):2209. http://dx.doi.org/10.3390/w13162209.

[34] Moazeni F, Khazaei J. Optimal operation of water-energy microgrids; A mixed integer linear programming formulation. J Clean Prod 2020;275:122776. http://dx.doi.org/10.1016/j.jclepro.2020.122776.

[35] Bischi A, Taccari L, Martelli E, Amaldi E, Manzolini G, Silva P, et al. A detailed MILP optimization model for combined cooling, heat and power system operation planning. Energy 2014;74:12–26. http://dx.doi.org/10.1016/j.energy.2014.02.042.

[36] Bussieck MR, Meeraus A. General algebraic modeling system (GAMS). In: Kallrath J, editor. Modeling languages in mathematical optimization. Applied optimization, vol. 88, Boston, MA: Springer US; 2004, p. 137–57. http://dx.doi.org/10.1007/978-1-4613-0215-5_8.

[37] Wächter A, Biegler LT. On the implementation of an interior-point filter line-search algorithm for large-scale nonlinear programming. Math Program 2006;106(1):25–57. http://dx.doi.org/10.1007/s10107-004-0559-y.

[38] Viessmann Deutschland GmbH. Dampferzeuger – Effiziente Anlagen bis 31,5 t/h. 2018, URL https://www.viessmann.at/de/industrie/grosskessel/dampfkessel/hochdruck-dampferzeuger-vitomax-hs.html.

[39] Marina A, Spoelstra S, Zondag HA, Wemmers AK. An estimation of the European industrial heat pump market potential. Renew Sustain Energy Rev 2021;139:110545. http://dx.doi.org/10.1016/j.rser.2020.110545.

[40] European Wind Energy Association. The economics of wind energy. 2009, URL https://windeurope.org/wp-content/uploads/files/about-wind/reports/Economics_of_Wind_Energy.pdf.

[41] EBSILON®Professional. URL https://help.ebsilon.com/EN/webframe.html#Component_119.html.

[42] Converse G, Griffin R. Extended parametric representation of compressor fans and turbines: Volume 1: CMGEN user's manual. URL https://ntrs.nasa.gov/citations/19860014465.

[43] Walsh PP, Fletcher P. Gas turbine performance. 2nd ed.. Malden, MA: Blackwell Science; 2008, http://dx.doi.org/10.1002/9780470774533, URL http://gbv.eblib.com/patron/FullRecord.aspx?p=239913.

[44] Verein Deutscher Ingenieure, editor. VDI-wärmeatlas. VDI-Buch, Imprint, Berlin, Heidelberg: Springer Vieweg; 2013.

[45] Cabeza LF. Advances in thermal energy storage systems: Methods and applications. 2nd ed.. Woodhead Publishing; 2020.

[46] Ding Y. Thermal energy storage: Materials, devices, systems and applications. Royal Society of Chemistry, University of Birmingham, UK; 2021.

[47] Dinker A, Agarwal M, Agarwal GD. Heat storage materials, geometry and applications: A review. J Energy Inst 2017;90(1):1–11. http://dx.doi.org/10.1016/j.joei.2015.10.002, URL https://www.sciencedirect.com/science/article/pii/S1743967115301215.

[48] Liu M, Saman W, Bruno F. Review on storage materials and thermal performance enhancement techniques for high temperature phase change thermal storage systems. Renew Sustain Energy Rev 2012;16(4):2118–32. http://dx.doi.org/10.1016/j.rser.2012.01.020, URL https://www.sciencedirect.com/science/article/pii/S1364032112000214.

[49] Laing D, Lehmann D. Concrete storage for solar thermal power plants and industrial process heat. In: IRES III, 3rd International Renewable Energy Storage Conference. 2008.

[50] Hoivik N, Greiner C, Tirado EB, Barragan J, Bergan P, Skeie G, et al. Demonstration of EnergyNest thermal energy storage (TES) technology. p. 080011. http://dx.doi.org/10.1063/1.4984432.
[51] Hoivik N, Greiner C, Barragan J, Iniesta AC, Skeie G, Bergan P, et al. Long-term performance results of concrete-based modular thermal energy storage system. J Energy Storage 2019;24:100735. http://dx.doi.org/10.1016/j.est.2019.04.009.
[52] Xu B, Li P-W, Chan CL. Extending the validity of lumped capacitance method for large Biot number in thermal storage application. Sol Energy 2012;86(6):1709–24. http://dx.doi.org/10.1016/j.solener.2012.03.016.
[53] Thiel C, Klapperich V. Heatcrete: Ein spezialbeton für die hochtemperaturwärmespeicherung. 2019, URL https://www.heidelbergcement.de/de/system/files_force/assets/document/energiewandel-regenerative-energiequellen-heatcrete-energynest-waermespeicher-waermetauschersaeulen-nlt28-2017.pdf.
[54] Therminol VP-1 technical bulletin. URL https://www.eastman.com/Literature_Center/T/TF9141.pdf.
[55] Dittus FW, Boelter L. Heat transfer in automobile radiators of the tubular type. Int Commun Heat Mass Transfer 1985;(12):3–22. http://dx.doi.org/10.1016/0735-1933(85)90003-X.
[56] Bauelos-Ruedas F, Angeles-Camacho C, Sebastin. Methodologies used in the extrapolation of wind speed data at different heights and its impact in the wind energy resource assessment in a region. In: Suvire GO, editor. Wind farm - Technical regulations, potential estimation and siting assessment. InTech; 2011, http://dx.doi.org/10.5772/20669.
[57] Deutscher Wetterdienst. Climate Data Center. URL https://opendata.dwd.de/climate_environment/CDC/.
[58] Vestas. 4MW platform brochure: V136-4.2 MW. URL https://www.vestas.com/en/products/4-mw-platform/v150-4_2_mw.
[59] Floors R, Nielsen M. Estimating air density using observations and re-analysis outputs for wind energy purposes. Energies 2019;12(11):2038. http://dx.doi.org/10.3390/en12112038.
[60] Hirth L, Mühlenpfordt J, Bulkeley M. The ENTSO-E transparency platform – A review of Europe's most ambitious electricity data platform. Appl Energy 2018;225:1054–67. http://dx.doi.org/10.1016/j.apenergy.2018.04.048.
[61] Icha P, Lauf T, Kuhs G. Entwicklung der spezifischen kohlendioxid-emissionen des deutschen strommix in den jahren 1990 - 2020: Climate change | 45/2021. 2021, URL https://www.umweltbundesamt.de/en/publikationen/entwicklung-der-spezifischen-kohlendioxid-7.
[62] Queipo NV, Haftka RT, Shyy W, Goel T, Vaidyanathan R, Tucker PK. Surrogate-based analysis and optimization. Prog Aerosp Sci 2005;41(1):1–28. http://dx.doi.org/10.1016/j.paerosci.2005.02.001.
[63] Bárkányi Á, Chován T, Németh S, Abonyi J. Modelling for digital twins—Potential role of surrogate models. Processes 2021;9(3):476. http://dx.doi.org/10.3390/pr9030476.
[64] McBride K, Sundmacher K. Overview of surrogate modeling in chemical process engineering. Chem Ing Tech 2019;91(3):228–39. http://dx.doi.org/10.1002/cite.201800091.
[65] Amaran S, Sahinidis NV, Sharda B, Bury SJ. Simulation optimization: A review of algorithms and applications. 4OR 2014;12(4):301–33. http://dx.doi.org/10.1007/s10288-014-0275-2.
[66] Montgomery DC. Design and Analysis of Experiments. 8th ed.. Hoboken, NJ: Wiley; 2013.
[67] Alizadeh R, Allen JK, Mistree F. Managing computational complexity using surrogate models: A critical review. Res Eng Des 2020;31(3):275–98. http://dx.doi.org/10.1007/s00163-020-00336-7.
[68] Otto M. Chemometrics: Statistics and computer application in analytical chemistry. 3rd ed.. Weinheim: Wiley-VCH Verlag GmbH & Co. KGaA; 2017.
[69] STATGRAPHICS centurion 19. 2022, URL https://www.statgraphics.com/.
[70] Gabrielli P, Gazzani M, Martelli E, Mazzotti M. Optimal design of multi-energy systems with seasonal storage. Appl Energy 2018;219:408–24. http://dx.doi.org/10.1016/j.apenergy.2017.07.142.
[71] Hoheisel T, Kanzow C, Schwartz A. Theoretical and numerical comparison of relaxation methods for mathematical programs with complementarity constraints. Math Program 2013;137(1–2):257–88. http://dx.doi.org/10.1007/s10107-011-0488-5.
[72] Bazaraa MS, Sherali HD, Shetty CM. Nonlinear programming. Hoboken, NJ, USA: John Wiley & Sons, Inc; 2006, http://dx.doi.org/10.1002/0471787779.
[73] Pardalos P, Tawarmalani M, Sahinidis NV. Convexification and global optimization in continuous and mixed-integer nonlinear programming. Vol. 65. Boston, MA: Springer US; 2002, http://dx.doi.org/10.1007/978-1-4757-3532-1.
[74] Li D, Xu X, Yu D, Dong M, Liu H. Rule based coordinated control of domestic combined micro-CHP and energy storage system for optimal daily cost. Appl Sci 2018;8(1):8. http://dx.doi.org/10.3390/app8010008.
[75] Clauß J, Stinner S, Sartori I, Georges L. Predictive rule-based control to activate the energy flexibility of norwegian residential buildings: Case of an air-source heat pump and direct electric heating. Appl Energy 2019;237:500–18. http://dx.doi.org/10.1016/j.apenergy.2018.12.074.
[76] Pinamonti M, Prada A, Baggio P. Rule-based control strategy to increase photovoltaic self-consumption of a modulating heat pump using water storages and building mass activation. Energies 2020;13(23):6282. http://dx.doi.org/10.3390/en13236282.
[77] COIN-OR Foundation I. Interior Point OPTimizer (IPOPT). URL https://github.com/coin-or/Ipopt.